Opportunistic UAV Navigation With Carrier Phase Measurements from Asynchronous Cellular Signals

Joe Khalife, *Student Member, IEEE,* and Zaher M. Kassas, *Senior Member, IEEE*

***Abstract*—This paper presents a framework for opportunistic unmanned aerial vehicle (UAV) navigation by exploiting carrier phase measurements from ambient cellular signals of opportunity. In the proposed framework, the cellular base transceiver stations (BTSs) are not assumed to be synchronous. A complete framework that employs an extended Kalman filter (EKF) is presented, including filter initialization and process and measurement noise covariance selection. The EKF estimates the position and velocity of the UAV as well as the differences between the UAV-mounted receiver and each of the BTSs' clock bias and clock drift. The observability of the estimation framework is analyzed and the boundedness of the EKF's errors is studied. A lower bound for the EKF estimation error covariance is derived, and it is shown that the covariance remains bounded. Monte Carlo simulations are conducted to study the effect of the number of BTSs, the initial UAV speed, and the receiver's oscillator quality, on the estimation performance. Two sets of experimental results are presented demonstrating UAVs navigating exclusively with cellular carrier phase measurements via the developed framework, achieving a total position root mean-squared error of 2.94 m and 5.99 m for UAV trajectories of 2.6 km and 2.9 km, respectively.**

***Index Terms*—Cellular signals, carrier phase, UAV, opportunistic navigation, observability, extended Kalman filter.**

I. Introduction

Current unmanned aerial vehicle (UAV) navigation systems will not meet the stringent requirements on accuracy, resiliency, and robustness due to their heavy reliance on jammable and spoofable global navigation satellite system (GNSS) signals [1], [2]. In addition to jamming and spoofing, unintentional interference or even the possible yet unlikely event of on-board GNSS receiver failure constitute major threats on safe and reliable UAV navigation. In such cases where GNSS signals are unusable, cellular signals of opportunity (SOPs) could be used for navigation either in (1) a standalone fashion [3], [4] or (2) an integrated fashion, aiding the UAV's inertial navigation system [5], [6]. Several receiver designs have been published recently, producing time-of-arrival (TOA) and frequency-of-arrival (FOA) measurements from cellular code-division multiple access (CDMA) and long-term evolution (LTE) signals [7]–[10]. Such measurements are typically used in navigation systems. Cellular signals are attractive for navigation since they are abundant, received at a much higher power than GNSS signals, possess a favorable horizontal geometry, and are free to use. Moreover, cellular signals received by UAVs do not suffer from severe multipath by virtue of the favorable channel between base stations and UAVs [11]. In fact, a recent study of UAV connectivity to the cellular network demonstrated that the received cellular signal power on low-altitude UAVs (30 m to 120 m) are stronger than the receiver power on ground-based receivers, despite the downwards-tilted cellular antennas [12]. The study attributes these findings to the fact that "free space propagation conditions at altitude more than make up for antenna gain reductions".

While TOA- and FOA-based navigation approaches are well-studied in the literature [13], [14], applying such approaches to cellular CDMA base transceiver stations (BTSs) or LTE eNodeBs requires perfect synchronization assumptions [15], [16]. However, cellular CDMA and LTE networks are not perfectly synchronized, and their protocols recommend synchronization of CDMA BTSs and LTE eNodeBs to within 3 microseconds from GPS time [17], [18]. This translates to ranging errors of about 900 meters. Several approaches in the literature have been proposed to account for the BTSs' or eNodeBs' clock biases and drifts, including using the round-trip time (RTT) instead of the TOA [19]. Although RTT-based methods could yield good results in asynchronous systems, two-way communication between the receiver and the BTSs or eNodeBs is needed. This limits the availability of RTT measurements to only paying subscribers to a particular cellular provider and compromises the privacy of the user. Some of the proposed navigation frameworks assume the BTSs' or eNodeBs' clock bias and drift to be constant [3], [20]. However, the clock bias and drift are dynamic and stochastic [21]; hence, must be continuously estimated.

To deal with this challenge, a framework employing a monitor receiver was put forth by [22]. Moreover, a mapper/navigator framework was proposed in [23], where the mapper, which was assumed to have complete knowledge of its states (e.g., by having access to GNSS signals), is estimating the clock states of BTSs in its environment, and is sharing these estimates with a navigating receiver that has no knowledge of its own states, but is making pseudorange measurements on the same BTSs in the environment. The mapper/navigator framework could yield centimeter-accurate UAV navigation when carrier phase observables extracted from cellular signals are exploited [24]. Having a mapper may be impractical in some environments or in the absence of a communication channel between the mapper and navigator. To alleviate the need of a monitor or a mapper in the case of code phase measurements from cellular signals, the navigator could

This work was supported in part by the Office of Naval Research (ONR) under Grant N00014-16-1-2305 and in part by the National Science Foundation (NSF) under Grant 1751205.

J. Khalife is with the department of Electrical Engineering and Computer Science (EECS) at the University of California, Irvine (UCI), USA. Z. M. Kassas is with Department of Mechanical and Aerospace Engineering and holds a joint appointment with the EECS Department at UCI. Address: 27 E Peltason Dr, Irvine, CA 92617, USA (email: khalifej@uci.edu and zkassas@ieee.org).

estimate its states simultaneously with the states (position, clock bias, and clock drift) of the BTSs in the environment, i.e., perform radio simultaneous localization and mapping (radio SLAM) [5], [25], [26]. Alternatively, in the case where the navigating UAV is making carrier phase measurements from cellular signals, the relative frequency stability of cellular CDMA BTSs or LTE eNodeBs, which approaches that of an atomic standard, may be leveraged. It was shown that sophisticated measurement models that capture this stability may be employed to achieve centimeter-accurate navigation solutions without a mapper [24]. However, this method may fail if the frequency stability requirement is not met.

This paper considers UAV navigation with cellular carrier phase measurements without any assumptions on the synchronization between cellular BTSs or eNodeBs nor on their relative frequency stability. Five contributions are subsequently presented. First, a framework for UAV navigation with carrier phase measurements from cellular SOPs is presented, which employs an extended Kalman filter (EKF). The precision of carrier phase measurements is on the order of the carrier signal wavelength, making such measurements attractive for UAV navigation. Second, the EKF initialization is discussed. Third, the EKF estimation error and estimation error covariance are analyzed, by studying the observability of the system under consideration as well as the EKF's stochastic stability. As a result, the study presented herein can be generalized to a broader class of problems: EKF-based navigation using SOP carrier phase and pseudorange measurements. Fourth, Monte Carlo (MC) simulations are conducted to demonstrate the theoretical predictions about the system and study the effect of (1) the number of available BTSs and/or eNodeBs available, (2) the initial UAV speed, and (3) the UAV-mounted receiver's clock quality, on the estimation performance. Fifth, two sets of experimental results are presented demonstrating UAVs navigating with the proposed framework achieving a root mean-squared error (RMSE) of 2.94 m and 5.99 m for UAV trajectories of 2.6 km and 2.9 km, respectively.

The remainder of the paper is organized as follows. Section II describes the cellular SOP and receiver dynamics models and the cellular carrier phase observable. Section III describes the EKF-based navigation framework. Section IV gives theoretical background on observability and boundedness of the EKF error state. Section V analyzes the observability and the EKF error boundedness of the proposed framework. Section VI characterizes the performance of the proposed framework through MC simulations. Section VII provides experimental results demonstrating meter-level UAV navigation accuracy. Concluding remarks are given in Section VIII.

II. Model Description

This section presents the dynamics model of the UAV-mounted receiver and cellular SOP as well as the cellular carrier phase measurement model. Note that an altimeter could be used to estimate the UAV's altitude. Therefore, only the UAV's two-dimensional (2–D) position is estimated in this paper. The subsequent analysis is readily extendable to 3–D; however, the vertical position estimate will suffer from large uncertainty due to the poor vertical diversity of cellular towers.

A. Cellular SOP Dynamics Model

The cellular SOPs emanate from spatially-stationary terrestrial BTSs or eNodeBs, and their states will consist of their *known* 2–D positions and *unknown* clock error states, namely the clock bias and clock drift. For simplicity of notation, let the term BTS denote any type of cellular SOP transmitter (CDMA BTS, LTE eNodeB, etc.), unless explicitly stated otherwise. The position vector of the n-th BTS is given by $\boldsymbol{r}_{s_n} = [x_{s_n}, y_{s_n}]^\mathsf{T}$. The state of the n-th BTS will only consist of its clock error state and is given by $\boldsymbol{x}_{\mathrm{clk},s_n}(k) \triangleq \left[c\delta t_{s_n}(k), c\dot{\delta} t_{s_n}(k)\right]^\mathsf{T}$, where $\delta t_{s_n}(k)$ and $\dot{\delta} t_{s_n}(k)$ are the clock bias and clock drift at time-step k, respectively, and c is the speed-of-light. The n-th BTS's dynamics can be described by the discretized state space model

$$\boldsymbol{x}_{\mathrm{clk},s_n}(k+1) = \mathbf{F}_{\mathrm{clk}}\, \boldsymbol{x}_{\mathrm{clk},s_n}(k) + \boldsymbol{w}_{\mathrm{clk},s_n}(k), \quad k = 0, 1, \ldots,$$

where $n = 1, \ldots, N$, with N being the total number of BTSs, and $\boldsymbol{w}_{\mathrm{clk},s_n}$ is a zero-mean white noise sequence with covariance $\mathbf{Q}_{\mathrm{clk},s_n}$, with

$$\mathbf{F}_{\mathrm{clk}} = \begin{bmatrix} 1 & T \\ 0 & 1 \end{bmatrix}, \; \mathbf{Q}_{\mathrm{clk},s_n} = c^2 \begin{bmatrix} S_{\tilde{w}_{\delta t_{s,n}}} T + S_{\tilde{w}_{\dot{\delta} t_{s,n}}} \frac{T^3}{3} & S_{\tilde{w}_{\dot{\delta} t_{s,n}}} \frac{T^2}{2} \\ S_{\tilde{w}_{\dot{\delta} t_{s,n}}} \frac{T^2}{2} & S_{\tilde{w}_{\dot{\delta} t_{s,n}}} T \end{bmatrix},$$

where T is the sampling time and $S_{\tilde{w}_{\delta t_{s,n}}}$ and $S_{\tilde{w}_{\dot{\delta} t_{s,n}}}$ are the power spectra of the continuous-time process noise driving the clock bias and clock drift, respectively. These spectra can be related to the power-law coefficients $\{h_\alpha\}_{\alpha=-2}^{2}$, which have been shown through laboratory experiments to be adequate to characterize the power spectral density of the fractional frequency deviation $y(t)$ of an oscillator from nominal frequency, which takes the form $S_y(f) = \sum_{\alpha=-2}^{2} h_\alpha f^\alpha$ [27]. It is common to approximate the clock error dynamics by considering only the frequency random walk coefficient h_{-2} and the white frequency coefficient h_0, which leads to $S_{\tilde{w}_{\delta t_{s,n}}} \approx \frac{h_{0,s_n}}{2}$ and $S_{\tilde{w}_{\dot{\delta} t_{s,n}}} \approx 2\pi^2 h_{-2,s_n}$ [28].

B. UAV-Mounted Receiver Dynamics Model

The UAV-mounted receiver state consists of its unknown position $\boldsymbol{r}_r(k) \triangleq [x_r(k), y_r(k)]^\mathsf{T}$, velocity $\dot{\boldsymbol{r}}_r(k)$, and clock error states $\boldsymbol{x}_{\mathrm{clk},r}(k) \triangleq \left[c\delta t_r(k), c\dot{\delta} t_r(k)\right]^\mathsf{T}$. Hence, the state vector of the receiver is given by $\boldsymbol{x}_r(k) = \left[\boldsymbol{r}_r^\mathsf{T}(k),\, \dot{\boldsymbol{r}}_r^\mathsf{T}(k),\, \boldsymbol{x}_{\mathrm{clk},r}^\mathsf{T}(k)\right]^\mathsf{T}$. The receiver's position $\boldsymbol{r}_r(k)$ and velocity $\dot{\boldsymbol{r}}_r(k)$ will be assumed to evolve according to a velocity random walk model [29]. Therefore, the UAV-mounted receiver dynamics is modeled according to the discretized model

$$\boldsymbol{x}_r\,(k+1) = \mathbf{F}_r\, \boldsymbol{x}_r(k) + \boldsymbol{w}_r(k), \quad k = 0, 1, \ldots,$$

where $\boldsymbol{w}_r = \left[\boldsymbol{w}_{\mathrm{pv}}^\mathsf{T}, \boldsymbol{w}_{\mathrm{clk},r}^\mathsf{T}\right]^\mathsf{T}$ is a discrete-time zero-mean white noise sequence with covariance $\mathbf{Q}_r = \mathrm{diag}\left[\mathbf{Q}_{\mathrm{pv}}, \mathbf{Q}_{\mathrm{clk},r}\right]$, with

$$\mathbf{F}_r = \begin{bmatrix} \mathbf{I}_{2\times 2} & T\mathbf{I}_{2\times 2} & \mathbf{0}_{2\times 2} \\ \mathbf{0}_{2\times 2} & \mathbf{I}_{2\times 2} & \mathbf{0}_{2\times 2} \\ \mathbf{0}_{2\times 2} & \mathbf{0}_{2\times 2} & \mathbf{F}_{\mathrm{clk}} \end{bmatrix}, \quad \mathbf{F}_{\mathrm{clk}} = \begin{bmatrix} 1 & T \\ 0 & 1 \end{bmatrix}$$

$$\mathbf{Q}_{\mathrm{clk},r}=c^2\begin{bmatrix} S_{\tilde{w}_{\delta t_r}}T+S_{\tilde{w}_{\dot{\delta} t_r}}\frac{T^3}{3} & S_{\tilde{w}_{\dot{\delta} t_r}}\frac{T^2}{2} \\ S_{\tilde{w}_{\dot{\delta} t_r}}\frac{T^2}{2} & S_{\tilde{w}_{\dot{\delta} t_r}}T \end{bmatrix}$$

$$\mathbf{Q}_{\mathrm{pv}}=\begin{bmatrix} \tilde{q}_x\frac{T^3}{3} & 0 & \tilde{q}_x\frac{T^2}{2} & 0 \\ 0 & \tilde{q}_y\frac{T^3}{3} & 0 & \tilde{q}_y\frac{T^2}{2} \\ \tilde{q}_x\frac{T^2}{2} & 0 & \tilde{q}_xT & 0 \\ 0 & \tilde{q}_y\frac{T^2}{2} & 0 & \tilde{q}_yT \end{bmatrix},$$

where $\tilde{q}_x$ and $\tilde{q}_y$ are the power spectral densities of the continuous-time x and y acceleration noise, respectively. The spectra $S_{\tilde{w}_{\delta t_r}}$ and $S_{\tilde{w}_{\dot{\delta} t_r}}$ are modeled similarly to the BTS spectra, but with receiver-specific $h_{0,r}$ and $h_{-2,r}$.

C. Cellular Carrier Phase Measurement Model

A specialized navigation receiver (e.g., [3], [7], [9], [10]) could produce a carrier phase observable to the n-th BTS given by

$$\phi_n(t)=\phi_n(t_0)+\int_{t_0}^{t} f_{D,n}(\tau)d\tau, \quad n=1,\ldots,N, \tag{1}$$

where $\phi_n(t_0)$ is the carrier phase at an initial time t_0 and $f_{D,n}(\tau)$ is the Doppler frequency at time τ. The carrier phase observable in (1) could be parameterized in terms of the receiver and BTS states to yield the discrete-time measurement model given by

$$\begin{aligned} z_n(k) &\triangleq \lambda\phi_n(t_0+kT) \\ &= \left\|\boldsymbol{r}_r(k)-\boldsymbol{r}_{s_n}\right\|_2 + c\left[\delta t_r(k)-\delta t_{s_n}(k)\right] \\ &\quad + \lambda N_n + v_n(k), \end{aligned} \tag{2}$$

where λ is the wavelength of the carrier signal, N_n represents the carrier phase ambiguity corresponding to the n-th BTS (namely, the initial phase difference between the receiver and the n-th BTS), and v_n is the measurement noise, which is modeled as a discrete-time zero-mean white Gaussian sequence with variance $\sigma_n^2(k)$. Note that the measurements are uncorrelated in time because it is assumed that (1) the sampling time is larger than the channel coherence time and (2) the channels between the UAV and the cellular BTSs are multipath-free. The second practical assumption is made since a strong line of sight component is usually observed in the received signal [12].

III. Navigation with Cellular SOP Carrier Phase Measurements

This section formulates an EKF-based framework for standalone navigation with carrier phase measurements from asynchronous BTSs.

A. Modified Clock Error States

Estimating the terms $c\delta t_r(k)$, $c\delta t_{s_n}(k)$, and λN_n in (2) individually is unnecessary; hence, they will be lumped into one bias term defined as

$$c\delta t_n(k)\triangleq c\left[\delta t_r(k)-\delta t_{s_n}(k)+\frac{\lambda}{c}N_n\right],$$

with an associated drift state $c\dot{\delta} t_n$ given by

$$c\dot{\delta} t_n(k)\triangleq c\left[\dot{\delta} t_r(k)-\dot{\delta} t_{s_n}(k)\right].$$

One may subsequently conclude that the dynamics of $\boldsymbol{x}_{\mathrm{clk},n}(k)\triangleq\left[c\delta t_n(k), c\dot{\delta} t_n(k)\right]^{\mathsf{T}}$ is given by

$$\boldsymbol{x}_{\mathrm{clk},n}(k+1)=\mathbf{F}_{\mathrm{clk}}\,\boldsymbol{x}_{\mathrm{clk},n}(k)+\boldsymbol{w}_{\mathrm{clk},n}(k), \quad n=1,\ldots,N,$$

where $\boldsymbol{w}_{\mathrm{clk},n}$ is a discrete-time zero-mean white noise sequence with covariance $\mathbf{Q}_{\mathrm{clk},n}=\mathbf{Q}_{\mathrm{clk},r}+\mathbf{Q}_{\mathrm{clk},s_n}$. Note that now $\boldsymbol{w}_{\mathrm{clk},n}(k)$ and $\boldsymbol{w}_{\mathrm{clk},m}(k)$ are correlated, with

$$\mathbb{E}\left[\boldsymbol{w}_{\mathrm{clk},n}(k)\boldsymbol{w}_{\mathrm{clk},m}^{\mathsf{T}}(k)\right]=\begin{cases}\mathbf{Q}_{\mathrm{clk},n}, & \text{if } n=m,\\ \mathbf{Q}_{\mathrm{clk},r}, & \text{otherwise.}\end{cases}$$

B. EKF Model

The EKF estimates the UAV-mounted receiver's position and velocity and the modified clock error states for all BTSs, namely

$$\begin{aligned}\boldsymbol{x}(k)\triangleq\big[\,&\boldsymbol{r}_r^{\mathsf{T}}(k),\, c\delta t_1(k),\,\ldots,\, c\delta t_N(k),\\ &\dot{\boldsymbol{r}}_r^{\mathsf{T}}(k),\, c\dot{\delta} t_1(k),\,\ldots,\, c\dot{\delta} t_N(k)\,\big]^{\mathsf{T}}.\end{aligned}$$

Note that $\boldsymbol{x}(k)$ may be expressed as $\boldsymbol{x}(k)=\boldsymbol{\Pi}\boldsymbol{x}'(k)$, where $\boldsymbol{x}'(k)\triangleq\left[\boldsymbol{r}_r^{\mathsf{T}}(k),\dot{\boldsymbol{r}}_r^{\mathsf{T}}(k),\boldsymbol{x}_{\mathrm{clk},1}^{\mathsf{T}}(k),\ldots,\boldsymbol{x}_{\mathrm{clk},N}^{\mathsf{T}}(k)\right]^{\mathsf{T}}$ and $\boldsymbol{\Pi}$ is some permutation matrix that could be readily calculated. The EKF considers the system with the following dynamics and measurement model

$$\boldsymbol{x}(k+1)=\mathbf{F}\boldsymbol{x}(k)+\boldsymbol{w}(k) \tag{3}$$

$$\boldsymbol{z}(k)=\boldsymbol{h}\left[\boldsymbol{x}(k)\right]+\boldsymbol{v}(k), \tag{4}$$

with $\boldsymbol{h}\left[\boldsymbol{x}(k)\right]\triangleq\left[h_1\left[\boldsymbol{x}(k)\right],\ldots,h_N\left[\boldsymbol{x}(k)\right]\right]^{\mathsf{T}}$, $h_n\left[\boldsymbol{x}(k)\right]\triangleq\left\|\boldsymbol{r}_r(k)-\boldsymbol{r}_{s_n}\right\|+c\delta t_n(k)$, $\boldsymbol{z}(k)\triangleq\left[z_1(k),\ldots,z_N(k)\right]^{\mathsf{T}}$, $\boldsymbol{w}$ is a discrete-time zero-mean white sequence with covariance $\mathbf{Q}\triangleq\boldsymbol{\Pi}\mathbf{Q}'\boldsymbol{\Pi}^{\mathsf{T}}$, where $\mathbf{Q}'\triangleq\mathrm{diag}\left[\mathbf{Q}_{\mathrm{pv}},\mathbf{Q}_{\mathrm{clk}}\right]$,

$$\mathbf{Q}_{\mathrm{clk}}\triangleq\begin{bmatrix}\mathbf{Q}_{\mathrm{clk},1} & \mathbf{Q}_{\mathrm{clk},r} & \cdots & \mathbf{Q}_{\mathrm{clk},r}\\ \mathbf{Q}_{\mathrm{clk},r} & \mathbf{Q}_{\mathrm{clk},2} & \cdots & \mathbf{Q}_{\mathrm{clk},r}\\ \vdots & \vdots & \ddots & \vdots\\ \mathbf{Q}_{\mathrm{clk},r} & \mathbf{Q}_{\mathrm{clk},r} & \cdots & \mathbf{Q}_{\mathrm{clk},N}\end{bmatrix},\quad \mathbf{F}\triangleq\begin{bmatrix}\mathbf{I}_{p\times p} & T\mathbf{I}_{p\times p}\\ \mathbf{0}_{p\times p} & \mathbf{I}_{p\times p}\end{bmatrix},$$

with $p=N+2$, and $\boldsymbol{v}\triangleq\left[v_{r_1},\ldots,v_n\right]^{\mathsf{T}}$ is a discrete-time zero-mean white Gaussian sequence with covariance $\mathbf{R}(k)\triangleq\mathrm{diag}\left[\sigma_1^2(k),\ldots,\sigma_N^2(k)\right]$. Section VII discusses how the process and measurement noise covariance matrices $\mathbf{Q}$ and $\mathbf{R}(k)$, respectively, are selected in a practical environment.

The EKF is producing an estimate $\hat{\boldsymbol{x}}(k|j)=\mathbb{E}\left[\boldsymbol{x}(k)|\,\boldsymbol{z}(1),\ldots,\boldsymbol{z}(j)\right]$, $j\le k$, with an associated estimation error covariance $\mathbf{P}(k|j)=\mathbb{E}\left[\tilde{\boldsymbol{x}}(k|j)\tilde{\boldsymbol{x}}^{\mathsf{T}}(k|j)\right]$, where $\tilde{\boldsymbol{x}}(k|j)\triangleq\boldsymbol{x}(k)-\hat{\boldsymbol{x}}(k|j)$ is the estimation error. The current state estimate $\hat{\boldsymbol{x}}(k|k)$ and its associated estimation error covariance $\mathbf{P}(k|k)$ are obtained using the standard EKF equations. The measurement Jacobian $\mathbf{H}(k)$ used in the EKF estimation error covariance update is given by

$$\mathbf{H}(k)=\left[\;\mathbf{G}(k)\quad\mathbf{I}_{N\times N}\quad\mathbf{0}_{(N+2)\times(N+2)}\;\right], \tag{5}$$

$$\mathbf{G}(k)\triangleq\left[\;\frac{\boldsymbol{r}_r(k)-\boldsymbol{r}_{s_1}}{\left\|\boldsymbol{r}_r(k)-\boldsymbol{r}_{s_1}\right\|}\quad\cdots\quad\frac{\boldsymbol{r}_r(k)-\boldsymbol{r}_{s_N}}{\left\|\boldsymbol{r}_r(k)-\boldsymbol{r}_{s_N}\right\|}\;\right]^{\mathsf{T}}, \tag{6}$$

where $\mathbf{G}(k)$ is evaluated at $\hat{\boldsymbol{x}}(k|k-1)$.

C. EKF Initialization

It is assumed that the UAV has access to GNSS signals at $k = 0$ and $k = 1$, from which it could estimate its position. These position estimates, denoted by $\boldsymbol{z}_{\boldsymbol{r}_r}(0)$ and $\boldsymbol{z}_{\boldsymbol{r}_r}(1)$, can be modeled as

$$\boldsymbol{z}_{\boldsymbol{r}_r}(j) = \boldsymbol{r}_r(j) + \boldsymbol{v}_{\boldsymbol{r}_r}(j), \quad j = 0, 1, \tag{7}$$

where $\boldsymbol{r}_r(j)$ is the UAV's true position and $\boldsymbol{v}_{\boldsymbol{r}_r}(j)$ is a random vector that captures the estimation uncertainty, which is modeled as a zero-mean white Gaussian random sequence with covariance $\boldsymbol{\Sigma}_{\boldsymbol{r}_r}(j)$. Moreover, During the same time GNSS signals are available, the receiver makes two consecutive carrier phase measurements to the N available BTSs prior to initializing the EKF, denoted by $\boldsymbol{z}(0)$ and $\boldsymbol{z}(1)$. Next, the maximum likelihood (ML) estimate of $\boldsymbol{x}(1)$ from $\boldsymbol{z}_{\rm ini} \triangleq \left[\boldsymbol{z}_{\boldsymbol{r}_r}^{\mathsf{T}}(1), \boldsymbol{z}_{\boldsymbol{r}_r}^{\mathsf{T}}(0), \boldsymbol{z}^{\mathsf{T}}(1), \boldsymbol{z}^{\mathsf{T}}(0)\right]^{\mathsf{T}}$ is formulated.

For a sufficiently small T, the receiver velocity at $k = 1$ may be expressed as

$$\dot{\boldsymbol{r}}_r(1) = \frac{1}{T}\left[\boldsymbol{r}_r(1) - \boldsymbol{r}_r(0)\right], \tag{8}$$

and the n-th BTS's clock drift at $k = 1$ as

$$c\dot{\delta}t_n(1) \approx \frac{1}{T}\left[c\delta t_n(1) - c\delta t_n(0)\right]. \tag{9}$$

From (8) and (9), one may express $\boldsymbol{x}(0)$ as

$$\boldsymbol{x}(0) = \mathbf{F}^{-1}\boldsymbol{x}(1). \tag{10}$$

Using (4), (7), and (10), the following measurement equation is obtained

$$\boldsymbol{z}_{\rm ini} = \boldsymbol{h}_{\rm ini}\left[\boldsymbol{x}(1)\right] + \boldsymbol{v}_{\rm ini}, \tag{11}$$

where the vector-valued function $\boldsymbol{h}_{\rm ini}$ is given by

$$\boldsymbol{h}_{\rm ini}\left[\boldsymbol{x}(1)\right] = \begin{bmatrix} \boldsymbol{r}_r(1) \\ \boldsymbol{r}_r(1) - T\dot{\boldsymbol{r}}_r(1) \\ \boldsymbol{h}\left[\boldsymbol{x}(1)\right] \\ \boldsymbol{h}\left[\mathbf{F}^{-1}\boldsymbol{x}(1)\right] \end{bmatrix},$$

and the measurement noise vector is given

$$\boldsymbol{v}_{\rm ini} = \left[\boldsymbol{v}_{\boldsymbol{r}_r}^{\mathsf{T}}(1),\ \boldsymbol{v}_{\boldsymbol{r}_r}^{\mathsf{T}}(0),\ \boldsymbol{v}^{\mathsf{T}}(1),\ \boldsymbol{v}^{\mathsf{T}}(0)\right]^{\mathsf{T}},$$

which is a zero-mean white Gaussian random vector with the block-diagonal covariance matrix $\boldsymbol{\Sigma}_{\rm ini} = \operatorname{diag}\left[\boldsymbol{\Sigma}_{\boldsymbol{r}_r}(1), \boldsymbol{\Sigma}_{\boldsymbol{r}_r}(0), \mathbf{R}(1), \mathbf{R}(0)\right]$. The ML estimate of $\boldsymbol{x}(1)$ can be therefore obtained from (11) according to

$$\hat{\boldsymbol{x}}_{\rm ML_{ini}} = \underset{\boldsymbol{x}(1)}{\operatorname{argmax}}\ \Lambda\left[\boldsymbol{z}_{\rm ini}; \boldsymbol{x}(1)\right], \tag{12}$$

where $\Lambda\left[\boldsymbol{z}_{\rm ini}; \boldsymbol{x}(1)\right]$ is the likelihood function of $\boldsymbol{z}_{\rm ini}$ parameterized by $\boldsymbol{x}(1)$, which is the multivariate Gaussian probability density function with zero-mean and covariance $\boldsymbol{\Sigma}_{\rm ini}$. The maximization problem in (12) is equivalent to

$$\hat{\boldsymbol{x}}_{\rm ML_{ini}} = \underset{\boldsymbol{x}(1)}{\operatorname{argmin}} \left\{\boldsymbol{z}_{\rm ini} - \boldsymbol{h}_{\rm ini}[\boldsymbol{x}(1)]\right\}^{\mathsf{T}} \boldsymbol{\Sigma}_{\rm ini}^{-1} \left\{\boldsymbol{z}_{\rm ini} - \boldsymbol{h}_{\rm ini}[\boldsymbol{x}(1)]\right\},$$

which can be solved using the Gauss-Newton method. It can be shown that

$$\hat{\boldsymbol{x}}_{\rm ML_{ini}} = \Big[\hat{\boldsymbol{r}}_{r,\rm ML_{ini}}^{\mathsf{T}},\ c\hat{\delta}t_{1,\rm ML_{ini}},\ \ldots,\ c\hat{\delta}t_{N,\rm ML_{ini}},\ \hat{\dot{\boldsymbol{r}}}_{r,\rm ML_{ini}}^{\mathsf{T}},\ c\hat{\dot{\delta}}t_{1,\rm ML_{ini}},\ \ldots,\ c\hat{\dot{\delta}}t_{N,\rm ML_{ini}}\Big]^{\mathsf{T}},$$

where

$$\hat{\boldsymbol{r}}_{r,\rm ML_{ini}} = \boldsymbol{z}_{\boldsymbol{r}_r}(1), \tag{13}$$

$$\hat{\dot{\boldsymbol{r}}}_{r,\rm ML_{ini}} = \frac{1}{T}\left[\boldsymbol{z}_{\boldsymbol{r}_r}(1) - \boldsymbol{z}_{\boldsymbol{r}_r}(0)\right], \tag{14}$$

$$c\hat{\delta}t_{n,\rm ML_{ini}} = z_n(1) - d_{r,n}(1), \tag{15}$$

$$c\hat{\dot{\delta}}t_{n,\rm ML_{ini}} = \frac{1}{T}\left[z_n(1) - z_n(0) + d_{r,n}(0) - d_{r,n}(1)\right], \tag{16}$$

with $d_{r,n}(j) \triangleq \|\boldsymbol{z}_{\boldsymbol{r}_r}(j) - \boldsymbol{r}_{s_n}\|$ for $j = 0, 1$. It can also be shown that the estimation error covariance associated with $\hat{\boldsymbol{x}}_{\rm ML_{ini}}$ is given by

$$\mathbf{P}_{\rm ML_{ini}} = \mathbf{A}_{\rm ini}\boldsymbol{\Sigma}_{\rm ini}\mathbf{A}_{\rm ini}^{\mathsf{T}}, \tag{17}$$

where

$$\mathbf{A}_{\rm ini} \triangleq \begin{bmatrix} \mathbf{I}_{2\times 2} & \mathbf{0}_{2\times 2} & \mathbf{0}_{2\times N} & \mathbf{0}_{2\times N} \\ -\boldsymbol{h}_{r,1}^{\mathsf{T}}(1) & \mathbf{0}_{1\times 2} & \boldsymbol{e}_{N,1}^{\mathsf{T}} & \mathbf{0}_{1\times N} \\ \vdots & \vdots & \vdots & \vdots \\ -\boldsymbol{h}_{r,N}^{\mathsf{T}}(1) & \mathbf{0}_{1\times 2} & \boldsymbol{e}_{N,N}^{\mathsf{T}} & \mathbf{0}_{1\times N} \\ \frac{1}{T}\mathbf{I}_{2\times 2} & -\frac{1}{T}\mathbf{I}_{2\times 2} & \mathbf{0}_{2\times N} & \mathbf{0}_{2\times N} \\ -\frac{1}{T}\boldsymbol{h}_{r,1}^{\mathsf{T}}(1) & \frac{1}{T}\boldsymbol{h}_{r,1}^{\mathsf{T}}(0) & \frac{1}{T}\boldsymbol{e}_{N,1}^{\mathsf{T}} & -\frac{1}{T}\boldsymbol{e}_{N,1}^{\mathsf{T}} \\ \vdots & \vdots & \vdots & \vdots \\ -\frac{1}{T}\boldsymbol{h}_{r,N}^{\mathsf{T}}(1) & \frac{1}{T}\boldsymbol{h}_{r,N}^{\mathsf{T}}(0) & \frac{1}{T}\boldsymbol{e}_{N,N}^{\mathsf{T}} & -\frac{1}{T}\boldsymbol{e}_{N,N}^{\mathsf{T}} \end{bmatrix},$$

with $\boldsymbol{h}_{r,n}(j) \triangleq \frac{\boldsymbol{z}_{\boldsymbol{r}_r}(j) - \boldsymbol{r}_{s_n}}{d_{r,n}(j)}$ for $j = 0, 1$, and $\boldsymbol{e}_{N,n} \in \mathbb{R}^N$ is the standard basis vector consisting of a one at the n-th element and zeros elsewhere. Finally, the EKF is initialized with

$$\hat{\boldsymbol{x}}(1|1) \equiv \hat{\boldsymbol{x}}_{\rm ML_{ini}}, \qquad \mathbf{P}(1|1) \equiv \mathbf{P}_{\rm ML_{ini}},$$

and is run for $k \geq 1$.

Remark 1 . Let v_{r_1} and $\hat{v}_{r_1}$ denote the true initial speed and its estimate, respectively, and let $\boldsymbol{u}_{r_1}$ and $\hat{\boldsymbol{u}}_{r_1}$ denote the true initial velocity direction unit vector and its estimate, respectively. Moreover, let $\sigma_{v_{r_1}}^2$ and $\mathbf{P}_{\boldsymbol{u}_{r_1}}$ denote the initial variance and covariance of the initial estimation errors $\tilde{v}_{r_1} \triangleq v_{r_1} - \hat{v}_{r_1}$ and $\tilde{\boldsymbol{u}}_{r_1} \triangleq \boldsymbol{u}_{r_1} - \hat{\boldsymbol{u}}_{r_1}$, respectively. It is shown in Appendix A that

$$\sigma_{v_{r_1}}^2 \leq \frac{\lambda_{\max,\dot{\boldsymbol{r}}}}{T^2},\ \sigma_{\boldsymbol{u}_{r_1}}^2 \triangleq \left\|\mathbf{P}_{\boldsymbol{u}_{r_1}}\right\| \leq \frac{\lambda_{\max,\dot{\boldsymbol{r}}}}{\left\|\boldsymbol{r}_r(1) - \boldsymbol{r}_r(0)\right\|^2}, \tag{18}$$

where $\lambda_{\max,\dot{\boldsymbol{r}}}$ is a positive real number that only depends on $\bar{\boldsymbol{\Sigma}}_{\boldsymbol{r}_r} \triangleq \boldsymbol{\Sigma}_{\boldsymbol{r}_r}(0) + \boldsymbol{\Sigma}_{\boldsymbol{r}_r}(1)$. It can be seen from (18) that increasing T reduces the uncertainty in the initial speed estimate. Increasing $\|\boldsymbol{r}_r(1) - \boldsymbol{r}_r(0)\|$ improves the estimate of the initial velocity direction unit vector. Given $\boldsymbol{\Sigma}_{\boldsymbol{r}_r}(0)$ and $\boldsymbol{\Sigma}_{\boldsymbol{r}_r}(1)$, (18) may be used to choose an initial sampling time T and/or distance $\|\boldsymbol{r}_r(1) - \boldsymbol{r}_r(0)\|$ that guarantee that $\sigma_{v_{r_1}}^2$ and $\sigma_{\boldsymbol{u}_{r_1}}^2$ will be below a specified threshold. Regardless of the choice of T and $\|\boldsymbol{r}_r(1) - \boldsymbol{r}_r(0)\|$, the proposed initialization scheme will always yield an initial state estimate that is consistent with its initial estimation error covariance, which is important when initializing the EKF.

IV. Theoretical Background on Observability and EKF Estimation Error Bounds

This section provides relevant theoretical background on observability and EKF estimation error bounds.

A. Observability of Linear and Nonlinear Systems

Consider the discrete-time linear time-varying system

$$\boldsymbol{x}(k+1) = \mathbf{F}(k)\,\boldsymbol{x}(k) + \boldsymbol{\Gamma}(k)\,\boldsymbol{u}(k)\,, \tag{19}$$

$$\boldsymbol{y}(k) = \mathbf{H}(k)\,\boldsymbol{x}(k)\,, \tag{20}$$

where $\boldsymbol{x} \in \mathbb{R}^{n_x}$ is the system's state, $\boldsymbol{u} \in \mathbb{R}^{n_u}$ is the input, and $\boldsymbol{y} \in \mathbb{R}^{n_y}$ is the measurement.

Observability of the discrete-time linear time-varying system defined in (19)–(20) is usually determined by studying the rank of either the observability Gramian or the observability matrix. The following theorem states a necessary and sufficient condition for observability of linear time-varying systems through the l-step observability matrix.

Theorem IV.1. *[30] The discrete-time linear time-varying system defined in* (19)–(20) *is l-step observable if and only if the l-step observability matrix, defined as*

$$\boldsymbol{\mathcal{O}}\,(k, k+l) \triangleq \begin{bmatrix} \mathbf{H}\,(k) \\ \mathbf{H}\,(k+1)\,\boldsymbol{\Phi}\,(k+1,k) \\ \vdots \\ \mathbf{H}\,(k+l-1)\,\boldsymbol{\Phi}\,(k+l-1,k) \end{bmatrix} \tag{21}$$

is full rank, i.e., $\operatorname{rank}\left[\boldsymbol{\mathcal{O}}\,(k, k+l)\right] = n_x$. *The matrix function $\boldsymbol{\Phi}(k,j)$ is the discrete-time state transition matrix, which is defined as*

$$\boldsymbol{\Phi}\,(k,j) \triangleq \begin{cases} \mathbf{F}\,(k-1)\,\mathbf{F}\,(k-2)\cdots\mathbf{F}\,(j)\,, & k \geq j+1 \\ \mathbf{I}, & k = j. \end{cases}$$

Linear observability tools may be applied to nonlinear systems by linearizing the dynamics and measurements to obtain $\mathbf{F}(k)$, $\boldsymbol{\Gamma}(k)$, and $\mathbf{H}(k)$ [31]. The observability results in such case are only valid locally.

B. EKF Error Bounds

The following useful lemma establishes bounds on the Kalman filter's estimation error covariance.

Lemma IV.1. *[32] Consider the discrete-time linear time-varying stochastic system*

$$\boldsymbol{x}(k+1) = \mathbf{F}(k)\,\boldsymbol{x}(k) + \boldsymbol{\Gamma}(k)\,\boldsymbol{u}(k) + \boldsymbol{w}(k), \tag{22}$$

$$\boldsymbol{z}(k) = \mathbf{H}(k)\,\boldsymbol{x}(k) + \boldsymbol{v}(k), \tag{23}$$

where $\boldsymbol{x} \in \mathbb{R}^{n_x}$ is the system's state, $\boldsymbol{u} \in \mathbb{R}^{n_u}$ is the input, $\boldsymbol{w} \in \mathbb{R}^{n_x}$ is a zero-mean white sequence with covariance $\mathbf{Q}(k)$, $\boldsymbol{z} \in \mathbb{R}^{n_z}$ is the measurement, and $\boldsymbol{v} \in \mathbb{R}^{n_z}$ is a zero-mean white sequence with covariance $\mathbf{R}(k)$. Assume that $\boldsymbol{w}(k)$ and $\boldsymbol{v}(j)$ are uncorrelated for all k and j. Let $\mathbf{P}(k+1|k)$ be a solution to the matrix Riccati difference equation in the Kalman filter estimating the state of system (22)–(23) *given by*

$$\begin{aligned}\mathbf{P}(k+1|k) = \mathbf{F}(k)\,\big\{&\mathbf{P}(k|k-1) - \mathbf{P}(k|k-1)\mathbf{H}^{\mathsf{T}}(k)\cdot \\ &\left[\mathbf{H}(k)\mathbf{P}(k|k-1)\mathbf{H}^{\mathsf{T}}(k) + \mathbf{R}(k)\right]^{-1}\cdot \\ &\mathbf{H}(k)\mathbf{P}(k|k-1)\big\}\,\mathbf{F}^{\mathsf{T}}(k) + \mathbf{Q}(k).\end{aligned}$$

Let the following hold:

1) *There are real numbers $\underline{q}, \bar{q}, \underline{r}, \bar{r} > 0$ such that $\mathbf{Q}(k)$ and $\mathbf{R}(k)$ are bounded by*

$$\underline{q}\mathbf{I} \preceq \mathbf{Q}(k) \preceq \bar{q}\mathbf{I}, \qquad \underline{r}\mathbf{I} \preceq \mathbf{R}(k) \preceq \bar{r}\mathbf{I}.$$

2) *The matrices $\mathbf{F}(k)$ and $\mathbf{H}(k)$ satisfy the uniform observability condition.*
3) *The initial condition $\mathbf{P}(1|0)$ of the matrix Riccati difference equation in the Kalman filter is positive definite.*

Then, there are real numbers $\underline{p}, \bar{p} > 0$ such that $\mathbf{P}(k+1|k)$ is bounded via

$$\underline{p}\mathbf{I} \preceq \mathbf{P}(k+1|k) \preceq \bar{p}\mathbf{I}, \qquad \forall\, k > 0.$$

Next, theoretical background on EKF estimation error bounds is provided. Consider the discrete-time nonlinear stochastic system

$$\boldsymbol{x}(k+1) = \boldsymbol{f}\left[\boldsymbol{x}(k), \boldsymbol{u}(k)\right] + \boldsymbol{w}(k) \tag{24}$$

$$\boldsymbol{z}(k) = \boldsymbol{h}\left[\boldsymbol{x}(k)\right] + \boldsymbol{v}(k), \tag{25}$$

where $\boldsymbol{x} \in \mathbb{R}^{n_x}$ is the system's state, $\boldsymbol{u} \in \mathbb{R}^{n_u}$ is the input, $\boldsymbol{w} \in \mathbb{R}^{n_x}$ is a zero-mean white sequence with covariance $\mathbf{Q}(k)$, $\boldsymbol{z} \in \mathbb{R}^{n_z}$ is the measurement, and $\boldsymbol{v} \in \mathbb{R}^{n_z}$ is a zero-mean white sequence with covariance $\mathbf{R}(k)$.

An EKF is employed to estimate $\boldsymbol{x}(k)$. Define the EKF linearization errors

$$\begin{aligned}\boldsymbol{\varphi}(k) \triangleq\ & \boldsymbol{f}\left[\boldsymbol{x}(k), \boldsymbol{u}(k)\right] - \boldsymbol{f}\left[\hat{\boldsymbol{x}}(k|k), \boldsymbol{u}(k)\right] \\ & - \mathbf{F}(k)\left[\boldsymbol{x}(k) - \hat{\boldsymbol{x}}(k|k)\right]\end{aligned} \tag{26}$$

$$\begin{aligned}\boldsymbol{\chi}(k) \triangleq\ & \boldsymbol{h}\left[\boldsymbol{x}(k)\right] - \boldsymbol{h}\left[\hat{\boldsymbol{x}}(k+1|k)\right] \\ & - \mathbf{H}(k)\left[\boldsymbol{x}(k) - \hat{\boldsymbol{x}}(k+1|k)\right],\end{aligned} \tag{27}$$

where $\mathbf{F}(k)$ and $\mathbf{H}(k)$ are the dynamics and observation Jacobians, respectively, evaluated at $\hat{\boldsymbol{x}}(k|k)$ and $\hat{\boldsymbol{x}}(k+1|k)$, respectively.

Definition IV.1. *[33] The stochastic sequence $\tilde{\boldsymbol{x}}(k|k)$ is said to be exponentially bounded in mean square, if there are real numbers $\eta, \nu > 0$ and $0 < \vartheta < 1$ such that*

$$\mathbb{E}\left[\left\|\tilde{\boldsymbol{x}}(k|k)\right\|^2\right] \leq \eta\left\|\tilde{\boldsymbol{x}}(1|1)\right\|^2\vartheta^k + \nu \tag{28}$$

holds for every $k > 0$.

Definition IV.2. *[33] The stochastic sequence $\tilde{\boldsymbol{x}}(k|k)$ is said to be exponentially bounded with probability one, if*

$$\sup_{k>0}\left\|\tilde{\boldsymbol{x}}(k|k)\right\| < \infty \tag{29}$$

holds with probability one.

Theorem IV.2. *[33] Consider the system defined in* (24)–(25) *and consider an EKF estimating its state vector. Moreover, let the following assumptions hold*

1) *There are positive real numbers $\bar{f}, \bar{h}, \underline{p}, \bar{p}, \underline{q}, \underline{r} > 0$ such that the following bounds hold for every $k > 0$*

$$\left\|\mathbf{F}(k)\right\| \leq \bar{f} \tag{30}$$

$$\left\|\mathbf{H}(k)\right\| \leq \bar{h} \tag{31}$$

$$\underline{p}\mathbf{I} \preceq \mathbf{P}(k+1|k) \preceq \bar{p}\mathbf{I} \tag{32}$$

$$\underline{q}\mathbf{I} \preceq \mathbf{Q}(k) \tag{33}$$

$$\underline{r}\mathbf{I} \preceq \mathbf{R}(k). \tag{34}$$

2) *The matrix* $\mathbf{F}(k)$ *is nonsingular for every* $k > 0$.
3) *There are positive real numbers* $\epsilon_\varphi, \epsilon_\chi, \kappa_\varphi, \kappa_\chi > 0$ *such that the nonlinear functions* $\boldsymbol{\varphi}(k)$ *and* $\boldsymbol{\chi}(k)$ *are bounded via*

$$\|\boldsymbol{\varphi}(k)\| \leq \kappa_\varphi \|\tilde{\boldsymbol{x}}(k|k)\|^2 \tag{35}$$

$$\|\boldsymbol{\chi}(k)\| \leq \kappa_\chi \|\tilde{\boldsymbol{x}}(k|k)\|^2, \tag{36}$$

with $\|\tilde{\boldsymbol{x}}(k|k)\| \leq \epsilon_\varphi$ *and* $\|\tilde{\boldsymbol{x}}(k|k)\| \leq \epsilon_\chi$.

Then, the estimation error $\tilde{\boldsymbol{x}}(k|k)$ *is exponentially bounded in mean square and bounded with probability one as per Definitions IV.1 and IV.2, respectively, provided that (i) the initial estimation error satisfies*

$$\|\tilde{\boldsymbol{x}}(1|1)\| \leq \epsilon \tag{37}$$

and (ii) the covariance matrices of the noise terms are bounded via

$$\mathbf{Q}(k) \preceq \delta \mathbf{I}, \quad \mathbf{R}(k) \preceq \delta \mathbf{I}, \tag{38}$$

for some $\epsilon, \delta > 0$.

V. Observability and EKF Estimation Error Bounds Analyses

This section shows that the environment with the dynamics and observation model defined in (3)–(4) is observable for $N \geq 2$. Moreover, it shows that the EKF estimation error is exponentially bounded in the mean square sense and bounded with probability one. In the sequel, the following assumptions are made:

A1. The BTSs are not colocated nor are all collinear.
A2. The UAV is not stationary nor is moving along a trajectory that is collinear with the vector connecting its receiver with any of the BTSs.
A3. The UAV is at a minimum distance d from each BTS at all time, i.e., $\|\boldsymbol{r}(k) - \boldsymbol{r}_{s_n}\| \geq d$, $\forall\, k > 0$ and $\forall\, n = 1, \ldots, N$.

A. Observability Analysis

The observability of an environment comprising multiple receivers making pseudorange measurements on multiple BTSs, assuming different *a priori* knowledge scenarios was analyzed in [31]. The observability analysis utilized the l-step observability matrix of the linearized system and considered the observability of the *individual* clock biases and drifts $c\delta t_r(k)$, $c\dot{\delta} t_r(k)$, $\{c\delta t_{s_n}(k)\}_{n=1}^N$, and $\left\{c\dot{\delta} t_{s_n}(k)\right\}_{n=1}^N$.

In contrast, the system in (3)–(4) considers a single receiver making carrier phase measurements on multiple BTSs, where the individual clock biases and carrier phase ambiguities are lumped into a *single* bias term $\{c\delta t_n(k)\}_{n=1}^N$ and the drifts are also lumped into a *single* drift term $\left\{c\dot{\delta} t_n(k)\right\}_{n=1}^N$.

The observability results for the system defined in (3)–(4) is captured in the following theorem.

Theorem V.1. *Under assumptions A1 and A2, the system defined in* (3)–(4) *is completely* l*-step observable for* $l \geq 4$ *and* $N \geq 2$.

Proof. The linearization of the deterministic part of the system (3)–(4) into the form (19)–(20) yields

$$\mathbf{F}(k) \equiv \begin{bmatrix} \mathbf{I}_{(N+2)\times(N+2)} & T\mathbf{I}_{(N+2)\times(N+2)} \\ \mathbf{0}_{(N+2)\times(N+2)} & \mathbf{I}_{(N+2)\times(N+2)} \end{bmatrix}, \quad \boldsymbol{\Gamma}(k) \equiv \mathbf{0},$$

$$\mathbf{H}(k) \equiv \begin{bmatrix} \mathbf{H}_\xi(k) & \mathbf{0}_{N\times(N+2)} \end{bmatrix}, \quad \mathbf{H}_\xi(k) \triangleq [\mathbf{G}(k) \quad \mathbf{I}_{N\times N}].$$

In the following, it will be proven by construction that the l-step observability matrix $\boldsymbol{\mathcal{O}}(k, k+l)$ of the linearized system is full rank, i.e.,

$$\sum_{i=1}^{2L} \gamma_i \boldsymbol{\mathcal{O}}(k, k+l)\, \boldsymbol{e}_{2L,i} = \mathbf{0} \tag{39}$$

is satisfied *if and only if* $\gamma_i = 0$, $\forall\, i = 1, \ldots, 2L$, where $L = N + 2$ and $\boldsymbol{e}_{L,i} \in \mathbb{R}^L$ is the standard basis vector consisting of a one at the i-th element and zeros elsewhere. Note that since $\boldsymbol{\mathcal{O}}(k, k+l) \in \mathbb{R}^{l\cdot N\times 2(N+2)}$, then $l \geq 4$ always satisfies $l \cdot N \geq 2(N+2)$ for $N \geq 2$. Let $l = 4$. Subsequently, $\boldsymbol{\mathcal{O}}(k, k+4)$ may be expressed as

$$\boldsymbol{\mathcal{O}}(k, k+4) = \begin{bmatrix} \boldsymbol{\mathcal{O}}_{11} & \boldsymbol{\mathcal{O}}_{12} \\ \boldsymbol{\mathcal{O}}_{21} & \boldsymbol{\mathcal{O}}_{22} \end{bmatrix},$$

$$\boldsymbol{\mathcal{O}}_{11} \triangleq \begin{bmatrix} \mathbf{H}_\xi(k) \\ \mathbf{H}_\xi(k+1) \end{bmatrix}, \quad \boldsymbol{\mathcal{O}}_{21} \triangleq \begin{bmatrix} \mathbf{H}_\xi(k+2) \\ \mathbf{H}_\xi(k+3) \end{bmatrix},$$

$$\boldsymbol{\mathcal{O}}_{12} \triangleq \begin{bmatrix} \mathbf{0} \\ T\mathbf{H}_\xi(k+1) \end{bmatrix}, \quad \boldsymbol{\mathcal{O}}_{22} \triangleq \begin{bmatrix} 2T\mathbf{H}_\xi(k+2) \\ 3T\mathbf{H}_\xi(k+3) \end{bmatrix}.$$

The matrix $\boldsymbol{\mathcal{O}}_{11}$ may also be expressed as

$$\boldsymbol{\mathcal{O}}_{11} = \begin{bmatrix} \mathbf{G}(k) & \mathbf{I}_{N\times N} \\ \mathbf{G}(k+1) & \mathbf{I}_{N\times N} \end{bmatrix}. \tag{40}$$

Note that $\boldsymbol{\mathcal{O}}_{11} \in \mathbb{R}^{2N\times(N+2)}$. Moreover, the inequality $2N \geq N + 2$ holds, for $N \geq 2$. Therefore,

$$\operatorname{rank}[\boldsymbol{\mathcal{O}}_{11}] \leq N + 2. \tag{41}$$

From (40), it can be seen that $\operatorname{rank}[\boldsymbol{\mathcal{O}}_{11}] \geq N$. Moreover, for $N \geq 2$, and if A1 and A2 hold, then the $(N+1)$st and $(N+2)$nd rows of $\boldsymbol{\mathcal{O}}_{11}$ will be linearly independent from the first N rows and from each other, yielding

$$\operatorname{rank}[\boldsymbol{\mathcal{O}}_{11}] \geq N + 2. \tag{42}$$

Combining (41) and (42), it can be deduced that $\operatorname{rank}[\boldsymbol{\mathcal{O}}_{11}] = N + 2$. Similarly, it can be shown that $\operatorname{rank}[\boldsymbol{\mathcal{O}}_{21}] = N + 2$. Subsequently,

$$\sum_{i=1}^{L} \alpha_i \boldsymbol{\mathcal{O}}_{11} \boldsymbol{e}_{L,i} = \mathbf{0}, \qquad \sum_{i=1}^{L} \beta_i \boldsymbol{\mathcal{O}}_{21} \boldsymbol{e}_{L,i} = \mathbf{0},$$

are satisfied *if and only if* $\alpha_i = \beta_i = 0$, $\forall\, i = 1, \ldots, L$. Therefore, the equality

$$\sum_{i=1}^{L} \pi_i \mathbf{H}_\xi(k+j)\, \boldsymbol{e}_{L,i} = \mathbf{0}, \quad \forall\, j = 0, \ldots, 3 \tag{43}$$

is satisfied *if and only if* $\pi_i = 0$, $\forall\, i = 1, \ldots, L$.

The left-hand side of (39) can be expressed as

$$\sum_{i=1}^{2L} \gamma_i \boldsymbol{\mathcal{O}}\left(k, k+4\right) \boldsymbol{e}_{2L,i} = \left[\boldsymbol{\rho}_0^{\mathsf{T}}, \ldots, \boldsymbol{\rho}_3^{\mathsf{T}}\right]^{\mathsf{T}}, \tag{44}$$

$$\boldsymbol{\rho}_j \triangleq \sum_{i=1}^{L} \left(\gamma_i + jT\gamma_{L+i}\right) \mathbf{H}_{\xi}(k+j)\, \boldsymbol{e}_{L,i}, \tag{45}$$

where $j = 0, \ldots, 3$. It can be seen from (43) that $\boldsymbol{\rho}_j = \mathbf{0}$ for all $j = 0, \ldots, 3$ *if and only if*

$$\gamma_i + jT\gamma_{L+i} = 0, \ \forall\, i = 1, \ldots, L; \ \forall\, j = 0, \ldots, 3. \tag{46}$$

Since (46) holds for all $j = 0, \ldots, 3$, then evaluating (46) at $j = 0$ yields

$$\gamma_i = 0, \qquad \forall\, i = 1, \ldots, L. \tag{47}$$

Combining (46) and (47) for $j > 0$ yields

$$\gamma_{L+i} = 0, \qquad \forall\, i = 1, \ldots, L. \tag{48}$$

Equations (46)–(48) imply (39); therefore, $\boldsymbol{\mathcal{O}}(k, k+4)$ is full rank. Using Theorem IV.1, the system is observable. □

Remark 2 . Note that $\boldsymbol{\mathcal{O}}(k, k+l)$ is an $l \cdot N \times 2(N+2)$ matrix; hence, $\operatorname{rank}\left[\boldsymbol{\mathcal{O}}(k, k+l)\right] \leq \min\left\{l \cdot N, 2(N+2)\right\}$. Subsequently, one necessary condition for the observability matrix to be full rank is that $l \cdot N \geq 2(N+2)$, i.e., the UAV makes carrier phase measurements at l epochs to the N cellular BTSs. For $N \geq 2$, this condition is satisfied for $l \geq 4$. For $N \geq 4$, this condition is satisfied for $l \geq 3$.

Remark 3 . The result of Theorem V.1 is only valid locally and in a deterministic sense, i.e., with no process or measurement noise. However, this result can be extended to the stochastic system (24)–(25). Let the measurement Jacobian $\mathbf{G}(k)$ with respect to the position states (cf. (6)) be re-parameterized in terms of the bearing angles $\{\theta_n(k)\}_{n=1}^{N}$ between each BTS and the UAV according to

$$\mathbf{G}(k) = \begin{bmatrix} \cos\left[\theta_1(k)\right] & \ldots & \cos\left[\theta_N(k)\right] \\ \sin\left[\theta_1(k)\right] & \ldots & \sin\left[\theta_N(k)\right] \end{bmatrix}^{\mathsf{T}}.$$

The presence of process noise will yield new bearing angle trajectories $\theta_n'(k) = \theta_n(k) + \delta\theta_n(k)$, where $\delta\theta_n(k)$ is the bearing angle error due to process noise. With assumptions A.1 and A.2, the new bearing angles will not change the structure nor the rank of $\mathbf{H}(k)$ (cf.(5)), which will remain a combination of cosine and sine functions and other constants. This in turn will satisfy the observability condition of the system with process noise. More details can be found in [33] (Lemma 4.1) and [34] (Corollary 5.2).

Remark 4 . The velocity random walk model considered in this paper is simple yet informative enough to capture the UAV dynamics between the measurement updates of the EKF. In particular, the EKF will use this model to perform the time-update step, and for sufficiently small T, the UAV's dynamics model would not deviate drastically from this model. Nevertheless, this model may not necessarily cover the variety of flight modes that are achievable using typical rotary wing UAVs. To address this, one may employ a multiple model approach to estimate the UAV's state, with each model matched to a different flight mode [35]–[38]. The observability analysis presented in this paper can be performed for each of the dynamics model assumed by the multiple model filter, such as acceleration random walk, constant turn-rate, or even a stationary UAV. Theorem V.1 can be extended to study the observability of higher order UAV dynamics models (e.g., acceleration random walk, jerk random walk, etc. [29]) and higher order clock error dynamics models (e.g., three-state clock error dynamics comprising time, frequency, and frequency aging [39], [40]). It can be readily shown that the system becomes unobservable when the UAV stops.

B. Lower Bound on the EKF Estimation Error Covariance

The optimal geometric configuration of sensors (or navigation sources) around an emitter (or receiver) has been well studied in the literature [41], [42]. It was found that in the presence of independent and identically distributed measurement noise, the trace of the estimation error covariance in a nonlinear least-squares estimator is minimized when the end points of the unit line of sight vectors pointing from the receiver to each navigation source form a regular polygon around the receiver, i.e., $\theta_n = \frac{2\pi(n-1)}{N}$, $n = 1, \ldots, N \geq 3$ [43]. The aforementioned configuration will be referred to as the optimal configuration.

Although the system discussed in Subsection III-B is non-linear, one may devise a scenario for $N \geq 3$ that will define a lower bound on the estimation error covariance in the EKF. To this end, it is assumed that the optimal BTS configuration around the receiver is maintained at all time, implying that assumption A1 is satisfied. Assumption A2 implies that the measurement Jacobian can not be the same at all time. In order to satisfy A1 and A2 simultaneously, it is assumed that optimal configuration is maintained and that the BTSs rotate around the receiver on the unit circle by $2\pi/N$ at each time-step. Therefore, the optimal bearing angles at any given time-step k will be given by

$$\theta_n^{\star}(k) = \frac{2\pi \cdot \operatorname{mod}(n-1+k, N)}{N}, \ n = 1, \ldots, N, \ k = 1, \ldots,$$

where $\operatorname{mod}(\cdot, \cdot)$ is the modulo operator. Note that this parametrization is independent of the state. Therefore, the Riccati equation may be iterated off-line with the optimal configuration and measurement noise covariance $\mathbf{R}^{\star}(k) \equiv \lambda_{\min}\left[\mathbf{R}(k)\right]\mathbf{I}$ to produce a lower bound on the estimation error covariance for the EKF, denoted $\mathbf{P}_{\min}(k+1|k)$, from which a real number $\underline{p} > 0$ such that $\underline{p}\mathbf{I} \preceq \mathbf{P}_{\min}(k+1|k)$ can be deduced. Note that $\lambda_{\min}[\mathbf{A}]$ indicates the smallest eigenvalue of matrix $\mathbf{A}$. It is also important to note that while this scenario could never be physically realized, it is only used to define a lower bound on the estimation error covariance.

Remark 5 . The intuition behind obtaining this lower bound is explained next. Assume two configurations for N BTSs: (i) the optimal one and (ii) any other arbitrary configuration. Given the same prior for both configurations, i.e., $\mathbf{P}_{\mathrm{i}}(k|k) = \mathbf{P}_{\mathrm{ii}}(k|k)$, then $\mathbf{P}_{\mathrm{i}}(k+1|k) = \mathbf{P}_{\mathrm{ii}}(k+1|k)$, since the dynamics

are linear time-invariant. The covariance measurement updates can be expressed in the information form as

$$\mathbf{P}_{\mathrm{i}}^{-1}(k+1|k+1) = \mathbf{P}_{\mathrm{i}}^{-1}(k+1|k) + \frac{1}{\sigma^2}\mathbf{H}_{\mathrm{i}}^{\mathsf{T}}(k+1)\mathbf{H}_{\mathrm{i}}(k+1), \tag{49}$$

$$\mathbf{P}_{\mathrm{ii}}^{-1}(k+1|k+1) = \mathbf{P}_{\mathrm{ii}}^{-1}(k+1|k) + \frac{1}{\sigma^2}\mathbf{H}_{\mathrm{ii}}^{\mathsf{T}}(k+1)\mathbf{H}_{\mathrm{ii}}(k+1), \tag{50}$$

Since (i) is the optimal configuration,

$$\mathbf{H}_{\mathrm{i}}^{\mathsf{T}}(k+1)\mathbf{H}_{\mathrm{i}}(k+1) \succeq \mathbf{H}_{\mathrm{ii}}^{\mathsf{T}}(k+1)\mathbf{H}_{\mathrm{ii}}(k+1). \tag{51}$$

From (49)–(51), it can be seen that $\mathbf{P}_{\mathrm{i}}(k+1|k+1) \preceq \mathbf{P}_{\mathrm{ii}}(k+1|k+1)$. Repeating this recursion yields $\mathbf{P}_{\mathrm{i}}(k+j|k+j) \preceq \mathbf{P}_{\mathrm{ii}}(k+j|k+j)$ for all $j \geq 1$.

C. EKF Estimation Error Bounds Analysis

From the system defined in (3)–(4), it can be seen that $\mathbf{F}(k) = \mathbf{F}$ is nonsingular and

$$\|\mathbf{F}\| = 1, \tag{52}$$

for all $k \geq 0$. Moreover, from the definition of $\mathbf{Q}$ and $\mathbf{R}(k)$ in Subsection III-B, it can be seen that $\mathbf{Q}(k) = \mathbf{Q} \succ \mathbf{0}$ and $\mathbf{R}(k) \succ \mathbf{0}$; hence, there exist real numbers $\underline{q}, \underline{r} > 0$ such that

$$\mathbf{Q} \succeq \underline{q}\mathbf{I}, \qquad \mathbf{R}(k) \succeq \underline{r}\mathbf{I}, \tag{53}$$

for all $k > 0$. It was established in Theorem V.1 that the system is observable; hence, using Lemma IV.1, there exist real numbers $\underline{p}, \bar{p} > 0$ such that

$$\underline{p}\mathbf{I} \preceq \mathbf{P}(k+1|k) \preceq \bar{p}\mathbf{I}, \quad \forall\, k > 0. \tag{54}$$

An approach for obtaining $\underline{p}$ is given in Subsection V-B. Since the dynamics of the system in (3) are linear, then

$$\|\boldsymbol{\varphi}(k)\| = 0, \quad \forall\, k > 0. \tag{55}$$

The following two lemmas establish the rest of the conditions for Theorem IV.2 to hold.

Lemma V.1. *The 2-norm of the measurement Jacobian defined in* (5) *is bounded by*

$$\|\mathbf{H}(k)\| \leq \sqrt{N+1}, \tag{56}$$

for all $k > 0$.

Proof. Equation (56) follows from showing that

$$\mathbf{H}^{\mathsf{T}}(k)\mathbf{H}(k) \preceq (N+1)\mathbf{I}. \tag{57}$$

The matrix $\boldsymbol{\Delta} \triangleq (N+1)\mathbf{I} - \mathbf{H}^{\mathsf{T}}(k)\mathbf{H}(k)$ is expressed as

$$\boldsymbol{\Delta} = \begin{bmatrix} \mathbf{M} & \mathbf{0} \\ \mathbf{0} & (N+1)\mathbf{I} \end{bmatrix},$$
$$\mathbf{M} \triangleq \begin{bmatrix} (N+1)\mathbf{I} - \mathbf{G}^{\mathsf{T}}(k)\mathbf{G}(k) & -\mathbf{G}^{\mathsf{T}}(k) \\ -\mathbf{G}(k) & N\mathbf{I} \end{bmatrix},$$

which implies that (57) is satisfied when $\mathbf{M} \succeq \mathbf{0}$. Since $N\mathbf{I} \succ \mathbf{0}$, then $\mathbf{M}$ is positive semi-definite if the Schur complement of its bottom-right block given by

$$\mathbf{M}_{\mathrm{Schur}} \triangleq (N+1)\mathbf{I} - \mathbf{G}^{\mathsf{T}}(k)\mathbf{G}(k) - \frac{1}{N}\mathbf{G}^{\mathsf{T}}(k)\mathbf{G}(k),$$

is positive semi-definite. For any matrix $\mathbf{A}$, the following holds

$$\mathbf{A}^{\mathsf{T}}\mathbf{A} \preceq \mathrm{trace}\left[\mathbf{A}^{\mathsf{T}}\mathbf{A}\right]\mathbf{I}.$$

It can be readily shown that $\mathrm{trace}\left[\mathbf{G}^{\mathsf{T}}(k)\mathbf{G}(k)\right] = N$ for all $k \geq 0$. Subsequently,

$$\mathbf{M}_{\mathrm{Schur}} \succeq (N+1)\mathbf{I} - N\mathbf{I} - \mathbf{I} = \mathbf{0},$$

which implies that $\mathbf{M} \succeq \mathbf{0}$, yielding (57) and consequently (56). □

Lemma V.2. *Consider the system defined in* (3)–(4)*. If A3 holds, then*

$$\max_{1\leq n\leq N} \sup_{\boldsymbol{x}(k)} \|\mathrm{Hess}\ h_n\left[\boldsymbol{x}(k)\right]\| \leq \frac{1}{d}, \tag{58}$$

where Hess *denotes the Hessian operator.*

Proof. It can be readily shown that

$$\mathrm{Hess}\ h_n\left[\boldsymbol{x}(k)\right] = \frac{1}{\|\boldsymbol{r}_r(k) - \boldsymbol{r}_{s_n}\|}\mathrm{diag}\left[\mathbf{U}, \mathbf{0}_{(2N+2)\times(2N+2)}\right],$$

where $\mathbf{U} \triangleq \mathbf{I}_{2\times 2} - \boldsymbol{v}\boldsymbol{v}^{\mathsf{T}}$ and $\boldsymbol{v} \triangleq \frac{\boldsymbol{r}_r(k) - \boldsymbol{r}_{s_n}}{\|\boldsymbol{r}_r(k) - \boldsymbol{r}_{s_n}\|}$. It can be seen that the matrix $\mathbf{U}$ is an annihilator matrix and therefore its eigenvalues consist of ones and zeros. Subsequently,

$$\|\mathrm{Hess}\ h_n\left[\boldsymbol{x}(k)\right]\| = \frac{1}{\|\boldsymbol{r}_r(k) - \boldsymbol{r}_{s_n}\|}.$$

Since A3 holds, i.e., $\|\boldsymbol{r}_r(k) - \boldsymbol{r}_{s_n}\| \geq d$, then $\|\mathrm{Hess}\ h_n\left[\boldsymbol{x}(k)\right]\| \leq \frac{1}{d}$, which in turn implies (58). □

Using Taylor's theorem and Lemma V.2, it can be deduced that

$$\|\boldsymbol{\chi}(k)\| \leq \kappa_\chi \|\tilde{\boldsymbol{x}}(k|k)\|^2, \tag{59}$$

where $\kappa_\chi = \frac{1}{d}$ [33]. Now the main result for the EKF error bounds is stated.

Theorem V.2. *Consider the system defined in* (3)–(4) *whose state is being estimated using an EKF as described in Subsection III-B. If A1–A3 hold, then the EKF error* $\tilde{\boldsymbol{x}}(k|k)$ *is exponentially bounded in the mean square and bounded with probability one as per Definitions IV.1 and IV.2, respectively, assuming*

$$\|\tilde{\boldsymbol{x}}(1|1)\| \leq \epsilon, \quad \mathbf{R}(k) \preceq \delta\mathbf{I}, \quad \mathbf{Q} \preceq \delta\mathbf{I},$$

for some $\epsilon, \delta > 0$.

Proof. Combining (52)–(56), (59), and the fact that $\mathbf{F}$ is nonsingular, one can see that all the conditions of Theorem IV.2 are satisfied, from which one concludes that $\tilde{\boldsymbol{x}}(k|k)$ is exponentially bounded and bounded with probability one. □

VI. Simulation Results

This section presents simulations to analyze the performance of the proposed EKF framework by varying: (i) the number of available BTSs, (ii) the initial speed of the UAV, and (iii) the quality of the oscillator on-board the UAV. The simulation setup and settings are discussed first, then, the results are provided.

A. Simulation Setup

The simulated environment consisted of 12 BTSs from 2 cellular providers and is illustrated in Fig. 1. It can be seen that due to the cellular structure, the geometry between the UAV and BTSs is favorable. The cell size was picked to be 2 km, which is a typical value in semi-urban environments. Monte Carlo (MC) simulations were ran for different values of: (i) the number of available BTSs N, (ii) the initial speed of the UAV v_{r_1}, and (iii) the UAV-mounted receiver's clock states' process noise covariance $\mathbf{Q}_{\text{clk},r}$. The number of available BTSs N was varied in $N \in \{6, 8, 10, 12\}$. The initial speed of the UAV v_{r_1} was varied in $v_{r_1} \in \{4, 9, 13\}$ m/s. The process noise covariance of the UAV-mounted receiver's oscillator was varied to correspond to that of a temperature-compensated crystal oscillator (TCXO) and to that of an oven-controlled crystal oscillator (OCXO). Subsequently, 24 cases were simulated. The UAV's position and velocity and the UAV-mounted receiver's and BTSs' clock states were simulated using the dynamics discussed in Subsections II-B and II-A with a sampling time $T = 0.1$ s. The carrier phase measurement to each BTS was simulated according to (1) with $\lambda = 33.96$ cm, which corresponds to a wavelength dedicated for a cellular CDMA channel. The 3GPP2 protocol requires cellular BTSs to be synchronized within 3μs to GPS with a frequency stability of 50 ppb [17], [18]. It was assumed that the BTSs are equipped with OCXOs to meet these requirements [44], [45]. The EKF was initialized according to the framework in Subsection III-C. The simulation settings are summarized in Table I.

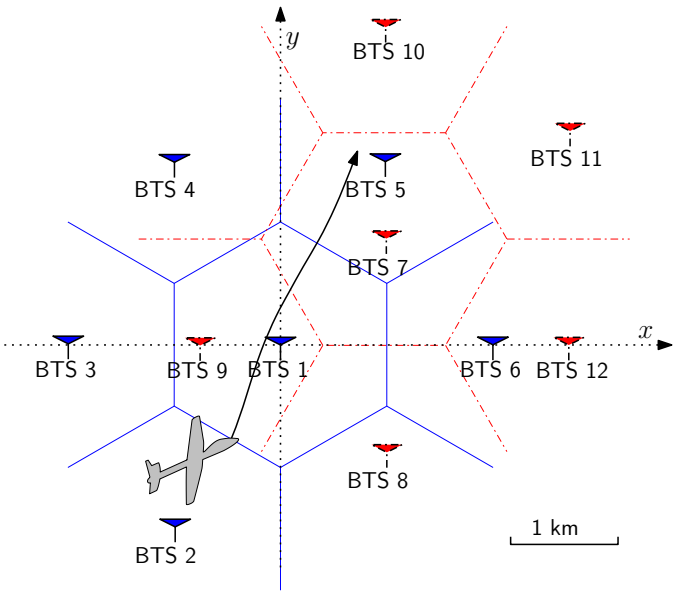

Fig. 1. Simulation environment layout. The blue and red colors represent cells and BTSs from 2 different cellular providers. The UAV's trajectory is shown in black.

B. Single Realization Simulation Results

A single realization of the EKF errors and associated $\pm 3\sigma$ bounds for the UAV's position and velocity and the clock error states corresponding to $c\delta t_1$ and $c\dot{\delta} t_1$ are plotted in Fig. 2 with $N = 10$, $v_{r_1} = 9$ m/s, and an OCXO-equipped receiver. The decreasing $\pm 3\sigma$ bounds and converging errors shown in Fig. 2 do not contradict the main results in Subsection V-C that the estimation error can be exponentially bounded and bounded with probability one, as per Definitions IV.1 and IV.2. Note that the remaining clock error states, namely $c\delta t_n$ and $c\dot{\delta} t_n$ for $n = 2, 3, \ldots, 9$, behave similarly to the ones plotted in Fig. 2.

TABLE I
SIMULATION SETTINGS

Parameter	Value	Unit
N	$\{6, 8, 10, 12\}$	-
λ	0.3396	m
T	0.1	s
$\mathbf{R}$	$(0.03) \cdot \mathbf{I}_{N\times N}$	m^2
$\mathbf{\Sigma}_{\boldsymbol{r}_r}(j)$	$\begin{bmatrix} 14.36 & -6.97 \\ -6.97 & 11.90 \end{bmatrix}$	m^2
j	$\{0, 1\}$	-
$\boldsymbol{r}_r(0)$	$[-500, -1500]^\mathsf{T}$	m
$\dot{\boldsymbol{r}}_r(0)$	$v_{r_1} \cdot [0.316, 0.949]^\mathsf{T}$	m/s
v_{r_1}	$\{4, 9, 13\}$	m/s
$h_{-2,r}$	$\{h_{-2,\text{TCXO}}, h_{-2,\text{OCXO}}\}$	s^{-1}
$h_{0,r}$	$\{h_{0,\text{TCXO}}, h_{0,\text{OCXO}}\}$	s
h_{-2,s_n}	$h_{-2,\text{OCXO}}$	s^{-1}
h_{0,s_n}	$h_{0,\text{OCXO}}$	s
$h_{-2,\text{TCXO}}$	2×10^{-20}	s^{-1}
$h_{-2,\text{OCXO}}$	4×10^{-23}	s^{-1}
$h_{0,\text{TCXO}}$	2×10^{-19}	s
$h_{0,\text{OCXO}}$	8×10^{-20}	s
$\tilde{q}_x, \tilde{q}_y$	0.03	m^2/s^3
$c\delta t_r, c\delta t_{s_n}$	$\mathcal{U}(-900, 900)^*$	m
$c\dot{\delta} t_r, c\dot{\delta} t_{s_n}$	$\mathcal{U}(-5, 5)$	m/s
N_n	$\mathcal{U}\{-500, 500\}^{**}$	cycles

* $\mathcal{U}(a, b)$ denotes the probability density function of a *continuous* uniformly-distributed random variable in (a, b).
** $\mathcal{U}\{c, d\}$ denotes the probability mass function of a *discrete* uniformly-distributed random variable in $[c, d]$.

C. Monte Carlo Simulation Results

Next, MC simulations were conducted by randomizing the process and measurement noise as well as the initial UAV position estimates $\hat{\boldsymbol{r}}_r(0)$ and $\hat{\boldsymbol{r}}_r(1)$. A total of 200 MC simulations were performed for each case described in Subsection VI-A. The total position RMSE and the final position error RMSE are tabulated in Table II.

The following can be deduced from Table II. First, as expected, the estimation performance improves as the number of available BTSs increases. Second, the receiver's clock quality significantly affects the estimation performance for $N \leq 10$. For $N > 10$, the effect of the receiver's oscillator quality becomes less significant. Third, as the initial speed increases, the estimation performance improves. Faster UAV speeds result in a faster change in the bearing angles between the UAV and the BTSs, yielding an increase in the amount of information coming from cellular carrier phase measurements.

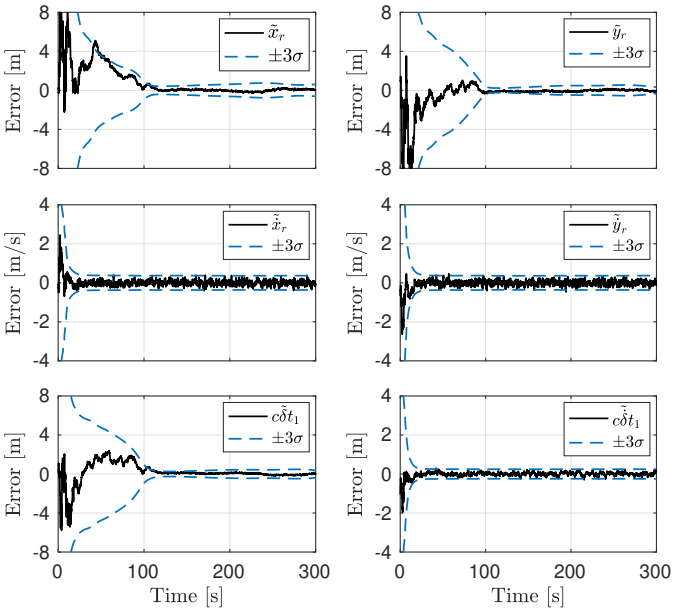

Fig. 2. Simulation results: Single realization of EKF errors and associated $\pm 3\sigma$ bounds for the UAV position and velocity and the clock error states corresponding to $c\delta t_1$ and $c\dot{\delta} t_1$ with $N = 10$, $v_{r_1} = 9$ m/s, and an OCXO-equipped receiver.

TABLE II
MC SIMULATION RESULTS

		Position RMSE (m)			Final position error (m)		
	N \ v_{r_1}	4	9	13	4	9	13
TCXO	6	33.47	22.85	13.15	14.28	10.23	7.29
	8	30.34	18.02	9.57	12.03	4.85	0.95
	10	27.96	17.25	9.84	9.69	4.94	1.09
	12	17.31	9.83	6.78	8.72	3.76	0.92
OCXO	6	25.97	14.84	11.18	10.15	9.65	6.52
	8	25.73	15.73	8.97	9.53	4.55	1.03
	10	24.77	13.77	5.50	8.80	2.58	0.48
	12	16.61	9.57	3.64	8.37	4.98	0.33

Next, the lower bound proposed in Subsection V-B is studied. To this end, 200 MC simulations were performed with $N = 10$, $v_{r_1} = 9$ m/s, and an OCXO-equipped receiver. The time history of the logarithm of the determinant of the estimation error covariance for each realization, denoted by $\text{logdet}\,[\mathbf{P}(k|k)]$, is plotted in Fig. 3 along with the logarithm of the determinant of the theoretical lower bound (LB) obtained according to Subsection V-B. Note that $\text{logdet}\,[\mathbf{P}(k|k)]$ is related to the volume of the uncertainty ellipsoid [46]. Moreover, The 1σ bound calculated by the EKF is plotted for each MC realization in Fig. 4 for the UAV's position and velocity as well as the clock error states corresponding to $c\delta t_1$ and $c\dot{\delta} t_1$. The theoretical LB calculated using the method proposed in Subsection V-B is also plotted. Note that the σ bounds of the remaining clock error states, namely $c\delta t_n$ and $c\dot{\delta} t_n$ for $n = 2, 3, \ldots, 9$, behave similarly to the ones plotted in Fig. 4.

The following can be concluded from these plots. First, the

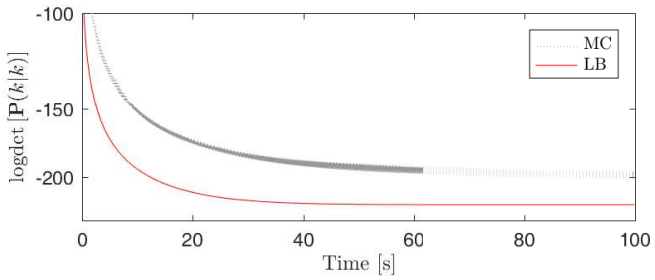

Fig. 3. MC simulation results: 200 realizations of $\text{logdet}\,[\mathbf{P}(k|k)]$ along with the logarithm of the determinant of the theoretical LB obtained according to Subsection V-B with $N = 10$, $v_{r_1} = 9$ m/s, and an OCXO-equipped receiver.

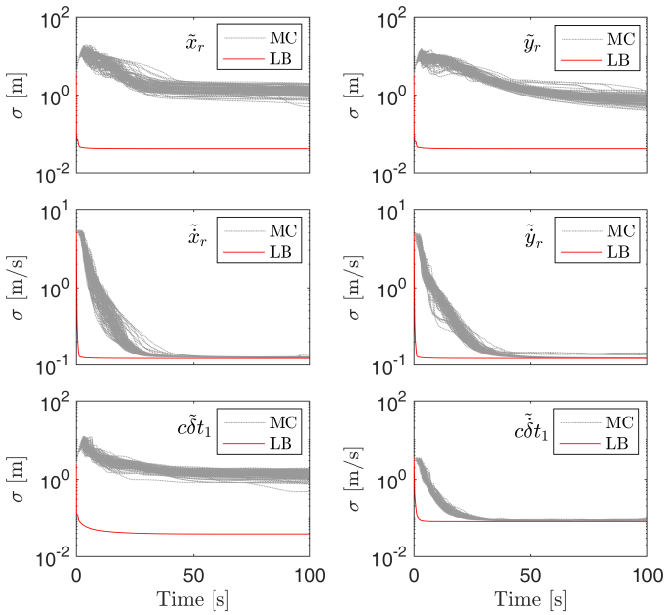

Fig. 4. MC simulation results: 200 realizations of 1σ bound for the UAV's position and velocity as well as the clock error states corresponding to $c\delta t_1$ and $\dot{\delta} t_1$, and the corresponding theoretical LB obtained according to Subsection V-B with $N = 10$, $v_{r_1} = 9$ m/s, and an OCXO-equipped receiver.

$\text{logdet}\,[\mathbf{P}(k|k)]$ plot in Fig. 3 shows that (i) the estimation error uncertainty is decreasing for all MC realizations and (ii) the theoretical LB is not violated. Second, each component of the theoretical LB in Fig. 4 bounds the respective component in the estimation error covariance. This result is not guaranteed to hold by the algorithm to compute the theoretical LB; however, it seems to hold. Third, the theoretical LB is tight for the velocity and clock drift states, but not tight for the position and clock bias states.

VII. EXPERIMENTAL RESULTS

In this section, two experiments are conducted demonstrating UAV navigation via the framework developed in this paper. In the following experiments, the altitude of the UAVs was known from their on-board navigation system.

A. Measurement Noise Statistics

The CDMA and LTE receivers employed in the experiments use second-order coherent phase lock loops (PLLs), for which it can be shown that the measurement noise variance σ_n^2 is

given by $\sigma_n^2(k) = \lambda^2 \frac{B_{\text{PLL}}}{C/N_{0_n}(k)}$, where B_{PLL} is the receiver's PLL noise equivalent bandwidth and $C/N_{0_n}(k)$ is the n-th BTS's carrier-to-noise ratio measured by the receiver [47]. In the following experiments, B_{PLL} was set to 3 Hz.

B. Hardware and Filter Description

An Autel Robotics X-Star Premium UAV was used for the first experiment and a DJI Matrice 600 was used for the second experiment. In each experiment, the UAVs were equipped with an Ettus E312 universal software radio peripheral (USRP), a consumer-grade 800/1900 MHz cellular antenna, and a small consumer-grade GPS antenna to discipline the on-board oscillator. In both experiments, the UAV-mounted receivers were tuned to listen to cellular signals in the two bands allocated for cellular communication in the U.S.: the 800 MHz and 1900 MHz bands. An E312 USRP was tuned to a 882.75 MHz carrier frequency (i.e., λ = 33.96 cm), which is a cellular CDMA channel allocated for the U.S. cellular provider Verizon Wireless. In the second experiment, the UAV was also equipped with a second antenna and another E312 USRP, which was tuned to a 1955 MHz carrier frequency (i.e., λ = 15.33 cm), which is an LTE channel allocated for the U.S. cellular provider AT&T. Samples of the received signals were stored for off-line post-processing. The cellular carrier phase measurements were given at a rate of 37.5 Hz, i.e., $T = 26.67$ ms. The ground-truth reference for each UAV trajectory was taken from its on-board navigation system, which uses GPS, an inertial measurement unit (IMU), and other sensors. The hovering horizontal precision of the UAVs are reported to be 2 meters for the X-Star Premium by Autel Robotics and 1.5 meters for the Matrice 600 by DJI. The E312 USRPs are equipped with TCXOs with $h_{0,r} = 2 \times 10^{-19}$ and $h_{-2,r} = 2 \times 10^{-20}$ and the BTSs are assumed to be equipped with OCXOs with $h_{0,s_n} = 8 \times 10^{-20}$ and $h_{-2,s_n} = 4 \times 10^{-23}$. The x and y continuous-time acceleration noise spectra were set to $\tilde{q}_x = \tilde{q}_y = 0.03$ m^2/s^3 for both experiments. The EKF was initialized according to the framework in Subsection III-C with initial position estimates obtained from the UAVs' on-board navigation systems. The experimental setup and BTS and eNodeB layout is shown in Fig. 5.

C. Experiment 1: UAV Navigation Results

In the first experiment, the UAV's total traversed trajectory was 2.6 km, which was completed in 4 minutes and 40 seconds. Over the course of the experiment, the UAV-mounted receiver was listening to 8 cellular CDMA BTSs as shown in Fig. 5 (denoted BTSs 1–8). The positions of the BTSs were obtained in two steps: 1) the framework described in [42] was used to obtain an initial map of the cellular BTS locations then 2) Google Earth was used to determine the final position of the BTSs. Fig. 6 shows the true and estimated UAV trajectories. The total position RMSE was found to be 2.94 m with a final estimation error at the end of the UAV's flight of 2.23 m. The EKF position error and the associated $\pm 3\sigma$ bounds as well as the position 1σ lower bound (LB) obtained according to Subsection V-B are shown in Fig. 7. In order to study the effect of the number of BTSs and their relative geometry, the EKF was run again using BTSs 1 through 4 ($N = 4$) and then BTSs 1 through 6 ($N = 6$). The resulting EKF position errors and the associated $\pm 3\sigma$ bounds as well as the position 1σ theoretical LB obtained according to Subsection V-B are shown in Fig. 8. The total position RMSEs and final errors are summarized in Table III.

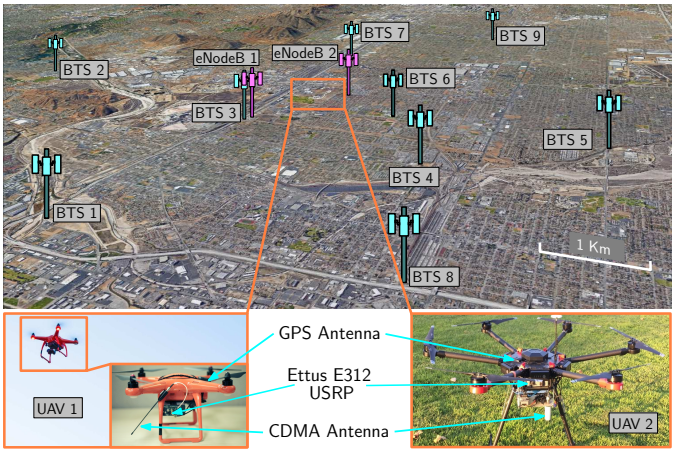

Fig. 5. Experimental setup and BTS and eNodeB layout. The environment consists of 9 cellular CDMA BTSs (cyan towers) and 2 LTE eNodeBs (magenta towers).

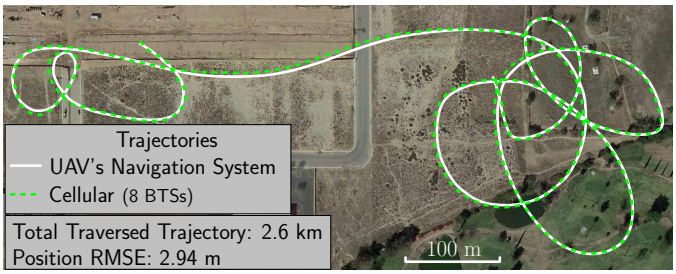

Fig. 6. Experiment 1 ($N = 8$): True UAV trajectory and estimated UAV trajectory via cellular carrier phase measurements with the proposed EKF framework. The true and estimated trajectories are shown in solid and dashed lines, respectively. Map data: Google Earth.

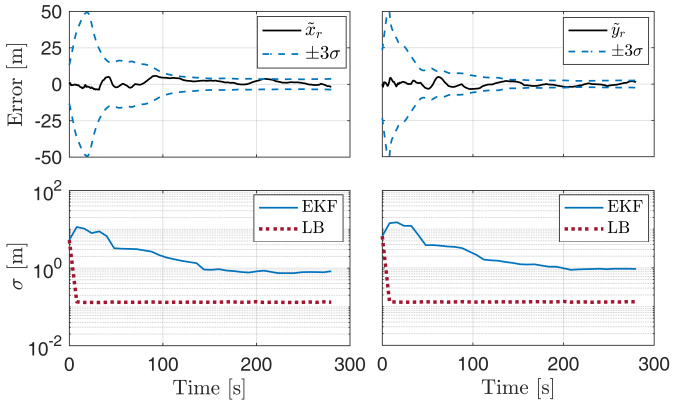

Fig. 7. Experiment 1 ($N = 8$): Top: UAV's position estimation error trajectories and associated $\pm 3\sigma$ bounds. Bottom: Position estimation error standard deviations and the theoretical LB obtained according to Subsection V-B.

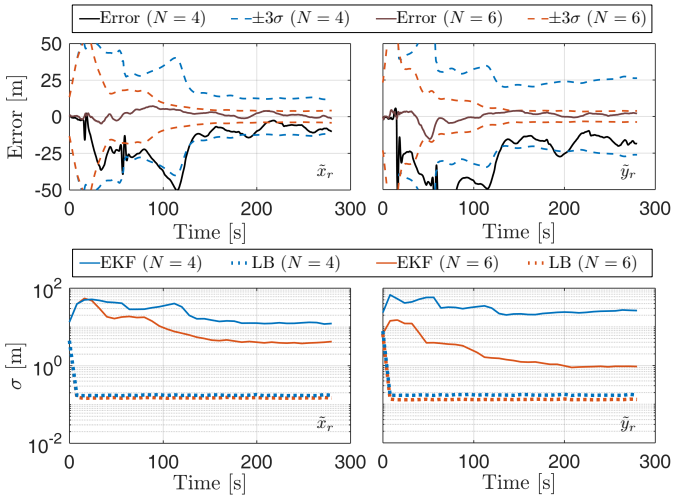

Fig. 8. Experiment 1 ($N = 4$ and $N = 6$): Top: UAV's position estimation error trajectories and associated $\pm 3\sigma$ bounds. Bottom: Position estimation error standard deviations and the theoretical LB obtained according to Subsection V-B.

D. Experiment 2: UAV Navigation Results

In the second experiment, the UAV's total traversed trajectory was 2.9 km, which was completed in 5 minutes. In this experiment, the receiver on-board the UAV was listening to 7 cellular CDMA BTSs and 2 LTE eNodeBs shown in Fig. 5. The BTS and eNodeB positions were determined the same way as in the first experiment. The true and estimated UAV trajectories are shown in Fig. 9. The total position RMSE was found to be 5.99 m with a final estimation error at the end of the UAV's flight of 3.46 m. The EKF position error and the associated $\pm 3\sigma$ bounds as well as the position 1σ lower bound (LB) obtained according to Subsection V-B are shown in Fig. 10. In order to study the effect of the number of BTSs and

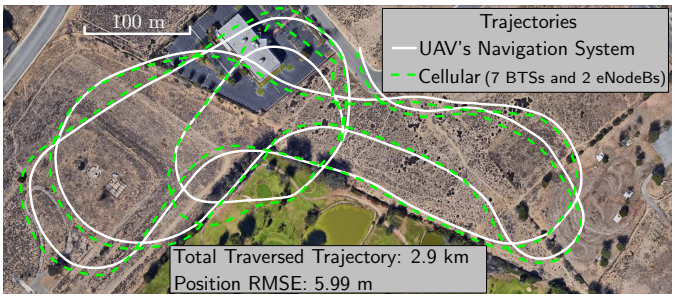

Fig. 9. Experiment 2 ($N = 9$): True UAV trajectory and estimated UAV trajectory via cellular carrier phase measurements with the proposed EKF framework. The true and estimated trajectories are shown in solid and dashed lines, respectively. Map data: Google Earth.

their relative geometry as in the first experiment, the EKF was run again using BTSs 1 through 4 ($N = 4$) and then BTSs 1 through 5 and eNodeB 1 ($N = 6$). The resulting EKF position errors and the associated $\pm 3\sigma$ bounds as well as the position 1σ theoretical LB obtained according to Subsection V-B are shown in Fig. 11. The total position RMSEs and final errors are summarized in Table III.

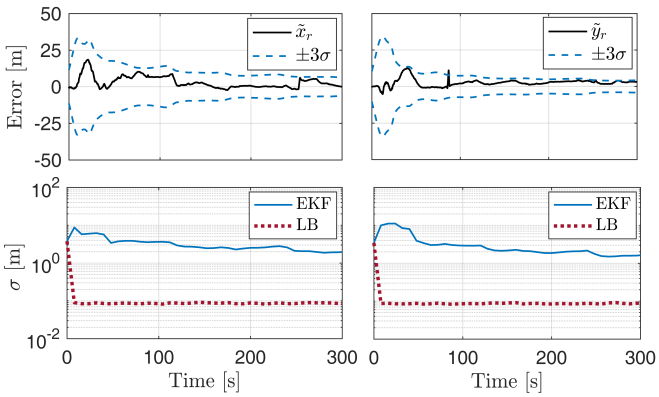

Fig. 10. Experiment 2 ($N = 9$): Top: UAV's position estimation error trajectories and associated $\pm 3\sigma$ bounds. Bottom: Position estimation error standard deviations and the theoretical LB obtained according to Subsection V-B.

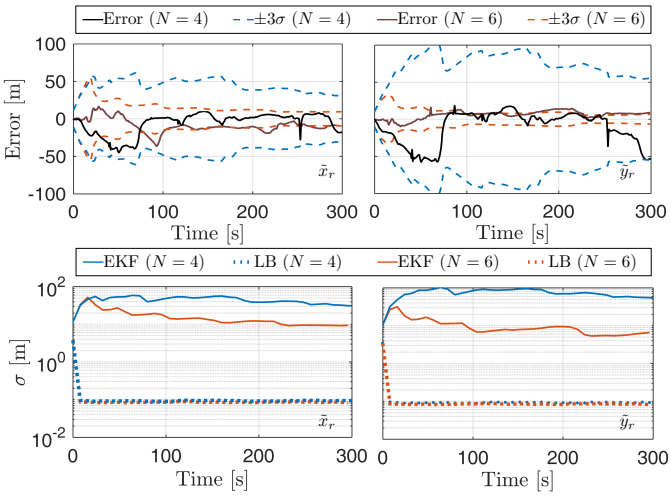

Fig. 11. Experiment 1 ($N = 4$ and $N = 6$): Top: UAV's position estimation error trajectories and associated $\pm 3\sigma$ bounds. Bottom: Position estimation error standard deviations and the theoretical LB obtained according to Subsection V-B.

TABLE III
EXPERIMENTAL RESULTS

	Experiment 1		Experiment 2	
N	Position RMSE (m)	Final position error (m)	Position RMSE (m)	Final position error (m)
4	37.39	21.29	30.77	39.81
6	4.68	2.41	14.96	12.84
8	2.94	2.23	-	-
9	-	-	5.99	3.46

E. Discussion

First, it is important to note that the favorable geometry of the BTSs and eNodeBs comes by virtue of (i) the cellular network structure where cells are typically organized in adjacent hexagons with servicing BTSs at the center of each hexagon and (ii) diversity of cellular providers. Moreover, since the wireless channel is particularly good for UAVs (line of sight is almost always maintained), it is very likely the UAV will be able to reliably listen to geometrically diverse BTSs, as shown

in Fig. 5.

Second, it was shown in Subsection V-C that the estimation error can be exponentially bounded and bounded with probability one, as per Definitions IV.1 and IV.2 respectively; and the estimation error covariance is bounded according to (54). None of the experiments contradicts this result since they both show a decreasing $\pm 3\sigma$ bounds and converging errors as shown in Fig. 7, Fig. 10, Fig. 8, and Fig. 11 without violating the proposed lower bound.

Third, the UAVs in both experiments were flying at almost constant speeds of 9.3 m/s and 9.7 m/s for experiments 1 and 2, respectively. Based on the simulation results presented in Section VI, the RMSE and final error are expected to decrease as the UAV speed increases.

Fourth, note that the proposed framework considers imperfect knowledge of the initial state (i.e., it is initialized with an initial estimate and corresponding uncertainty). It is important that the initial estimate be consistent with the initial estimation error covariance (uncertainty). The initialization scheme proposed in Subsection III-C ensures that the initial error and the initial uncertainty are consistent.

Fifth, the framework studied in this paper assumed the BTSs' positions to be known a priori with no uncertainty. Having uncertainty in the BTS's position does not guarantee the applicability of Theorem V.2. Future work could extend this work to the case with unknown/uncertain BTS positions. The reader is encouraged to look at the work in [5] and [26] for more details on how uncertainty in the BTS positions affects the performance of an opportunistic navigation framework.

Sixth, the UAV's on-board oscillator was disciplined using GPS signals during the experiment. The effect of not disciplining the on-board oscillator can be captured by increasing the clock process noise covariance matrix. Based on the results in Section VI, the RMSE and final error are expected to increase slightly when the on-board oscillator is not disciplined by GPS signals. It is important to note that now one has to find a new (ϵ, δ) pair for Theorem V.2 to hold. Since $\mathbf{Q}$ increases in a GPS-denied environment, then δ is likely to increase. Intuitively, one expects ϵ to decrease in this case for Theorem V.2 to hold. More details can be found in [33].

Remark 6 . The EKF employs statistical models to propagate the position and velocity of the UAV and the clock bias and drift differences. Such models will inherently mismatch the true dynamics of the UAV and clock states, possibly yielding large estimation errors. Using an IMU to propagate the position and velocity states of the UAV should yield better results [5]. Moreover, an adaptive filter may be employed to simultaneously estimate the clock states' process noise covariance to reduce the clock model mismatch [45].

VIII. Conclusion

This paper presented a framework for UAV navigation with asynchronous cellular signals. The framework employs precise cellular carrier phase measurements and an EKF to estimate the position and velocity of the UAV as well as the difference of the biases and drifts between the receiver's and each BTS's clock. An EKF initialization scheme was also proposed. Moreover, it was shown that (1) this framework is observable and (2) the EKF error state is asymptotically stable in a mean square sense and bounded with probability one. A lower bound for the EKF's estimation error covariance was provided. MC simulations showed that this bound is not violated and studied the performance of the proposed framework for varying (1) number of BTSs, (2) initial UAV speeds, and (3) UAV-mounted receiver clock qualities. It was also shown that the EKF estimation error covariance is upper bounded. Finding such an upper bound is involved and could be the subject of future work. Two sets of experimental results on two different UAVs showed that this framework can achieve 2.94 and 5.99 m position RMSE, over UAV trajectories of 2.6 km and 2.9 km, respectively.

Appendix A
Derivation of the Upper Bounds in (18)

In this appendix, the estimation error covariance associated with the initial speed estimate $\hat{v}_{r_1} \triangleq \left\| \hat{\dot{\boldsymbol{r}}}_{r,\mathrm{ML_{ini}}} \right\|$ and the initial velocity direction unit vector estimate $\hat{\boldsymbol{u}}_{r_1} \triangleq \frac{\hat{\dot{\boldsymbol{r}}}_{r,\mathrm{ML_{ini}}}}{\left\| \hat{\dot{\boldsymbol{r}}}_{r,\mathrm{ML_{ini}}} \right\|}$ are studied. Let $v_{r_1} \triangleq \|\dot{\boldsymbol{r}}_r(1)\|$ denote the true initial speed and $\boldsymbol{u}_{r_1} \triangleq \frac{\dot{\boldsymbol{r}}_r}{\|\dot{\boldsymbol{r}}_r\|}$ denote the true initial direction unit vector. Using first-order Taylor series expansion around $\dot{\boldsymbol{r}}_r(1)$, the initial speed estimate may be approximated with

$$\hat{v}_{r_1} \approx v_{r_1} - \boldsymbol{u}_{r_1}^{\mathsf{T}} \tilde{\dot{\boldsymbol{r}}}_{r,\mathrm{ini}}, \tag{60}$$

where $\tilde{\dot{\boldsymbol{r}}}_{r,\mathrm{ini}} \triangleq \dot{\boldsymbol{r}}_r(1) - \hat{\dot{\boldsymbol{r}}}_{r,\mathrm{ML_{ini}}}$. The initial speed estimation error can be calculated from (60) as

$$\tilde{v}_{r_1} \triangleq v_{r_1} - \hat{v}_{r_1} = \boldsymbol{u}_{r_1}^{\mathsf{T}} \tilde{\dot{\boldsymbol{r}}}_{r,\mathrm{ini}},$$

and its associated estimation error variance may obtained according

$$\sigma_{v_{r_1}}^2 \triangleq \mathbb{E}\left[\tilde{v}_{r_1}^2\right] = \boldsymbol{u}_{r_1}^{\mathsf{T}} \mathbb{E}\left[\tilde{\dot{\boldsymbol{r}}}_{r,\mathrm{ini}} \tilde{\dot{\boldsymbol{r}}}_{r,\mathrm{ini}}^{\mathsf{T}}\right] \boldsymbol{u}_{r_1}.$$

It can be shown from (14) and (17) that

$$\mathbf{P}_{\dot{r},\mathrm{ini}} \triangleq \mathbb{E}\left[\tilde{\dot{\boldsymbol{r}}}_{r,\mathrm{ini}} \tilde{\dot{\boldsymbol{r}}}_{r,\mathrm{ini}}^{\mathsf{T}}\right] = \frac{1}{T^2} \bar{\boldsymbol{\Sigma}}_{\boldsymbol{r}_r},$$

where $\bar{\boldsymbol{\Sigma}}_{\boldsymbol{r}_r} \triangleq \boldsymbol{\Sigma}_{\boldsymbol{r}_r}(0) + \boldsymbol{\Sigma}_{\boldsymbol{r}_r}(1)$. Since $\boldsymbol{u}_{r_1}$ is a unit vector, $\sigma_{v_{r_1}}^2$ may bounded according to

$$\sigma_{v_{r_1}}^2 \leq \frac{\lambda_{\max,\dot{r}}}{T^2}, \tag{61}$$

where $\lambda_{\max,\dot{r}}$ denotes the maximum eigenvalue of $\bar{\boldsymbol{\Sigma}}_{\boldsymbol{r}_r}$. Note that since $\bar{\boldsymbol{\Sigma}}_{\boldsymbol{r}_r}$ is positive definite, then $\lambda_{\max,\dot{r}}$ is a positive real number that only depends on $\bar{\boldsymbol{\Sigma}}_{\boldsymbol{r}_r}$.

Next, the estimation error covariance of $\hat{\boldsymbol{u}}_{r_1}$ is characterized. Using first-order Taylor series expansion around $\dot{\boldsymbol{r}}_r$, $\hat{\boldsymbol{u}}_{r_1}$ may be approximated with

$$\hat{\boldsymbol{u}}_{r_1} \approx \boldsymbol{u}_{r_1} - \boldsymbol{\Psi} \tilde{\dot{\boldsymbol{r}}}_{r,\mathrm{ini}}, \tag{62}$$

where $\boldsymbol{\Psi} \triangleq \frac{1}{v_{r_1}} \left(\mathbf{I}_{2\times 2} - \boldsymbol{u}_{r_1} \boldsymbol{u}_{r_1}^{\mathsf{T}}\right)$. The initial direction unit vector estimation error can be calculated from (62) as

$$\tilde{\boldsymbol{u}}_{r_1} \triangleq \boldsymbol{u}_{r_1} - \hat{\boldsymbol{u}}_{r_1} = \boldsymbol{\Psi} \tilde{\dot{\boldsymbol{r}}}_{r,\mathrm{ini}},$$

The matrix $\boldsymbol{\Psi}$ is an annihilator matrix; therefore, $\|\boldsymbol{\Psi}\| = 1$. The estimation error covariance associated with $\tilde{\boldsymbol{u}}_{r_1}$ is given by

$$\mathbf{P}_{\boldsymbol{u}_{r_1}} \triangleq \mathbb{E}\left[\tilde{\boldsymbol{u}}_{r_1}\tilde{\boldsymbol{u}}_{r_1}^{\mathsf{T}}\right] = \frac{1}{v_{r_1}^2}\boldsymbol{\Psi}\bar{\boldsymbol{\Sigma}}_{\boldsymbol{r}_r}\boldsymbol{\Psi}^{\mathsf{T}}. \tag{63}$$

Using (8) and (63), $\left\|\mathbf{P}_{\boldsymbol{u}_{r_1}}\right\|$ may be bounded according to

$$\sigma_{\boldsymbol{u}_{r_1}}^2 \triangleq \left\|\mathbf{P}_{\boldsymbol{u}_{r_1}}\right\| \leq \frac{\lambda_{\max,\dot{r}}}{\left\|\boldsymbol{r}_r(1) - \boldsymbol{r}_r(0)\right\|^2}. \tag{64}$$

ACKNOWLEDGMENT

The authors would like to thank Kimia Shamaei and Joshua Morales for their help in data collection.

REFERENCES

[1] M. Bryson and S. Sukkarieh, "Observability analysis and active control for airborne SLAM," *IEEE Transactions on Aerospace and Electronic Systems*, vol. 44, no. 1, pp. 261–280, January 2008.

[2] A. Kerns, D. Shepard, J. Bhatti, and T. Humphreys, "Unmanned aircraft capture and control via GPS spoofing," *Journal of Field Robotics*, vol. 31, no. 4, pp. 617–636, 2014.

[3] C. Yang, T. Nguyen, and E. Blasch, "Mobile positioning via fusion of mixed signals of opportunity," *IEEE Aerospace and Electronic Systems Magazine*, vol. 29, no. 4, pp. 34–46, April 2014.

[4] Z. Kassas, J. Khalife, K. Shamaei, and J. Morales, "I hear, therefore I know where I am: Compensating for GNSS limitations with cellular signals," *IEEE Signal Processing Magazine*, pp. 111–124, September 2017.

[5] J. Morales, P. Roysdon, and Z. Kassas, "Signals of opportunity aided inertial navigation," in *Proceedings of ION GNSS Conference*, September 2016, pp. 1492–1501.

[6] Z. Kassas, J. Morales, K. Shamaei, and J. Khalife, "LTE steers UAV," *GPS World Magazine*, vol. 28, no. 4, pp. 18–25, April 2017.

[7] J. del Peral-Rosado, J. Lopez-Salcedo, G. Seco-Granados, F. Zanier, P. Crosta, R. Ioannides, and M. Crisci, "Software-defined radio LTE positioning receiver towards future hybrid localization systems," in *Proceedings of International Communication Satellite Systems Conference*, October 2013, pp. 14–17.

[8] A. Mannesson, M. Yaqoob, B. Bernhardsson, and F. Tufvesson, "Tightly coupled positioning and multipath radio channel tracking," *IEEE Transactions on Aerospace and Electronic Systems*, vol. 52, no. 4, pp. 1522–1535, August 2016.

[9] J. Khalife, K. Shamaei, and Z. Kassas, "Navigation with cellular CDMA signals – part I: Signal modeling and software-defined receiver design," *IEEE Transactions on Signal Processing*, vol. 66, no. 8, pp. 2191–2203, April 2018.

[10] K. Shamaei, J. Khalife, and Z. Kassas, "Exploiting LTE signals for navigation: Theory to implementation," *IEEE Transactions on Wireless Communications*, vol. 17, no. 4, pp. 2173–2189, April 2018.

[11] J. Khalife and Z. Kassas, "Navigation with cellular CDMA signals – part II: Performance analysis and experimental results," *IEEE Transactions on Signal Processing*, vol. 66, no. 8, pp. 2204–2218, April 2018.

[12] Qualcomm Technologies, Inc., "LTE unmanned aircraft systems," Tech. Rep. 1.0.1, May 2017. [Online]. Available: https://www.qualcomm.com/documents/lte-unmanned-aircraft-systems-trial-report/

[13] D. Shin and T. Sung, "Comparisons of error characteristics between TOA and TDOA positioning," *IEEE Transactions on Aerospace and Electronic Systems*, vol. 38, no. 1, pp. 307–311, January 2002.

[14] L. Romero and J. Mason, "Geolocation using TOA, FOA, and altitude information at singular geometries," *IEEE Transactions on Aerospace and Electronic Systems*, vol. 51, no. 2, pp. 1069–1078, April 2015.

[15] N. Patwari, J. Ash, S. Kyperountas, A. Hero, R. Moses, and N. Correal, "Locating the nodes: cooperative localization in wireless sensor networks," *IEEE Signal Processing Magazine*, vol. 22, no. 4, pp. 54–69, July 2005.

[16] A. Tahat, G. Kaddoum, S. Yousefi, S. Valaee, and F. Gagnon, "A look at the recent wireless positioning techniques with a focus on algorithms for moving receivers," *IEEE Access*, vol. 4, pp. 6652–6680, 2016.

[17] 3GPP2, "Recommended minimum performance standards for cdma2000 spread spectrum base stations," 3rd Generation Partnership Project 2 (3GPP2), TS C.S0010-E, March 2014. [Online]. Available: http://www.arib.or.jp/english/html/overview/doc/STD-T64v7_00/Specification/ARIB_STD-T64-C.S0010-Ev2.0.pdf

[18] 3GPP, "Evolved universal terrestrial radio access (E-UTRA); requirements for support of radio resource management," 3rd Generation Partnership Project (3GPP), TS 36.133, April.

[19] J. Wennervirta and T. Wigren, "RTT positioning field performance," *IEEE Transactions on Vehicular Technology*, vol. 59, no. 7, pp. 3656–3661, September 2010.

[20] A. Yeredor, "On passive TDOA and FDOA localization using two sensors with no time or frequency synchronization," in *Proceedings of IEEE International Conference on Acoustics, Speech and Signal Processing*, May 2013, pp. 4066–4070.

[21] J. Barnes, A. Chi, R. Andrew, L. Cutler, D. Healey, D. Leeson, T. McGunigal, J. Mullen, W. Smith, R. Sydnor, R. Vessot, and G. Winkler, "Characterization of frequency stability," *IEEE Transactions on Instrumentation and Measurement*, vol. 20, no. 2, pp. 105–120, May 1971.

[22] K. Carter, R. Ramlall, M. Tummala, and J. McEachen, "Bandwidth efficient ATSC TDOA positioning in GPS-denied environments," in *Proceedings of ION International Technical Meeting Conference*, January 2013, pp. 717–725.

[23] J. Khalife, K. Shamaei, and Z. Kassas, "A software-defined receiver architecture for cellular CDMA-based navigation," in *Proceedings of IEEE/ION Position, Location, and Navigation Symposium*, April 2016, pp. 816–826.

[24] J. Khalife and Z. Kassas, "Precise UAV navigation with cellular carrier phase measurements," in *Proceedings of IEEE/ION Position, Location, and Navigation Symposium*, April 2018, pp. 978–989.

[25] Z. Kassas, "Collaborative opportunistic navigation," *IEEE Aerospace and Electronic Systems Magazine*, vol. 28, no. 6, pp. 38–41, 2013.

[26] J. Morales and Z. Kassas, "Information fusion strategies for collaborative radio SLAM," in *Proceedings of IEEE/ION Position Location and Navigation Symposium*, April 2018, pp. 1445–1454.

[27] A. Thompson, J. Moran, and G. Swenson, *Interferometry and Synthesis in Radio Astronomy*, 2nd ed. John Wiley & Sons, 2001.

[28] R. Brown and P. Hwang, *Introduction to Random Signals and Applied Kalman Filtering*, 3rd ed. John Wiley & Sons, 2002.

[29] X. Li and V. Jilkov, "Survey of maneuvering target tracking. Part I: Dynamic models," *IEEE Transactions on Aerospace and Electronic Systems*, vol. 39, no. 4, pp. 1333–1364, 2003.

[30] W. Rugh, *Linear System Theory*, 2nd ed. Upper Saddle River, NJ: Prentice Hall, 1996.

[31] Z. Kassas and T. Humphreys, "Observability analysis of collaborative opportunistic navigation with pseudorange measurements," *IEEE Transactions on Intelligent Transportation Systems*, vol. 15, no. 1, pp. 260–273, February 2014.

[32] B. Anderson and J. Moore, "Detectability and stabilisability of time-varying discrete-time linear systems," *SIAM Journal on Control and Optimiaztion*, vol. 19, pp. 20–32, 1981.

[33] K. Reif, S. Gunther, E. Yaz, and R. Unbehauen, "Stochastic stability of the discrete-time extended Kalman filter," *IEEE Transactions on Automatic Control*, vol. 44, no. 4, pp. 714–728, April 1999.

[34] T. Song and J. Speyer, "A stochastic analysis of a modified gain extended Kalman filter with applications to estimation with bearings only measurements," *IEEE Transactions on Automatic Control*, vol. 30, no. 10, pp. 940–949, October 1985.

[35] M. Yeddanapudi, Y. Bar-Shalom, and K. Pattipati, "IMM estimation for multitarget-multisensor air traffic surveillance," *Proceedings of the IEEE*, vol. 85, no. 1, pp. 80–96, January 1997.

[36] P. Hanlon and P. Maybeck, "Multiple-model adaptive estimation using a residual correlation Kalman filter bank," *IEEE Transactions on Aerospace and Electronic Systems*, vol. 36, no. 2, pp. 393–406, April 2000.

[37] Y. Bar-Shalom, X. Li, and T. Kirubarajan, *Estimation with Applications to Tracking and Navigation*. New York, NY: John Wiley & Sons, 2002.

[38] Z. Kowalczuk and M. Sankowski, "Soft- and hard-decision multiple-model estimators for air traffic control," *IEEE Transactions on Aerospace and Electronic Systems*, vol. 46, no. 4, pp. 2056–2065, October 2010.

[39] S. Stein and R. Filler, "Kalman filter analysis for real time applications of clocks and oscillators," in *Proceedings of the Frequency Control Symposium*, June 1988, pp. 447–452.

[40] C. Zucca and P. Tavella, "The clock model and its relationship with the Allan and related variances," *IEEE Transactions on Ultrasonics, Ferroelectrics, and Frequency Control*, vol. 52, no. 2, pp. 289–296, February 2005.
[41] C. Yang, L. Kaplan, E. Blasch, and M. Bakich, "Optimal placement of heterogeneous sensors for targets with Gaussian priors," *IEEE Transactions on Aerospace and Electronic Systems*, vol. 49, no. 3, pp. 1637–1653, July 2013.
[42] J. Morales and Z. Kassas, "Optimal collaborative mapping of terrestrial transmitters: receiver placement and performance characterization," *IEEE Transactions on Aerospace and Electronic Systems*, vol. 54, no. 2, pp. 992–1007, April 2018.
[43] N. Levanon, "Lowest GDOP in 2-D scenarios," *IEE Proceedings Radar, Sonar and Navigation*, vol. 147, no. 3, pp. 149–155, 2000.
[44] K. Wesson, K. Pesyna, J. Bhatti, and T. Humphreys, "Opportunistic frequency stability transfer for extending the coherence time of GNSS receiver clocks," in *Proceedings of ION GNSS Conference*, September 2010, pp. 2959–2968.
[45] Z. Kassas, V. Ghadiok, and T. Humphreys, "Adaptive estimation of signals of opportunity," in *Proceedings of ION GNSS Conference*, September 2014, pp. 1679–1689.
[46] Z. Kassas, A. Arapostathis, and T. Humphreys, "Greedy motion planning for simultaneous signal landscape mapping and receiver localization," *IEEE Journal of Selected Topics in Signal Processing*, vol. 9, no. 2, pp. 247–258, March 2015.
[47] P. Misra and P. Enge, *Global Positioning System: Signals, Measurements, and Performance*, 2nd ed. Ganga-Jamuna Press, 2010.

Joe Khalife (S'2015) is a Ph.D. candidate at the University of California, Irvine. He received a B.E. in Electrical Engineering and an M.S. in Computer Engineering from the Lebanese American University (LAU). From 2012 to 2015, he was a research assistant at LAU. He is a member of the Autonomous Systems Perception, Intelligence, and Navigation (ASPIN) Laboratory. His research interests include opportunistic navigation, autonomous vehicles, and software-defined radio.

Zaher (Zak) M. Kassas (S'98-M'08-SM'011) is an assistant professor at the University of California, Irvine and director of the ASPIN Laboratory. He received a B.E. in Electrical Engineering from LAU, an M.S. in Electrical and Computer Engineering from The Ohio State University, and an M.S.E. in Aerospace Engineering and a Ph.D. in Electrical and Computer Engineering from The University of Texas at Austin. In 2018, he received the National Science Foundation (NSF) Faculty Early Career Development Program (CAREER) award, and in 2019, he received the Office of Naval Research (ONR) Young Investigator Program (YIP) award. His research interests include cyber-physical systems, estimation theory, navigation systems, autonomous vehicles, and intelligent transportation systems.